Analysis of Band-Edge Dynamics in ZnO & MgZnO Thin Films

Presented in Partial Fulfillment of the Requirements for the Degree of

Master of Science

with a
Major in Physics

in the

College of Graduate Studies

University of Idaho

by

Amrah Canul

Major Professor
Leah Bergman, Ph.D.

Committee
Ruprecht Machleidt, Ph.D.
Matthew McCluskey, Ph.D.

Department Administrator
Ray von Wandruszka, Ph.D.

November 2015

Authorization to Submit Dissertation

This thesis of Amrah Canul, submitted for the degree of Master of Science with a Major in Physics and titled "Analysis of Band-Edge Dynamics in ZnO & MgZnO Thin Films," has been reviewed in final form. Permission, as indicated by the signatures and dates below, is now granted to submit final copies to the College of Graduate Studies for approval.

Major Professor:	Leah Bergman, Ph.D	11/11/15
Committee Members:	Ruprecht Machleidt, Ph.D	11/11/15
	Matthew McCluskey, Ph.D	11/11/15
Department Administrator:	Ray von Wandruszka, Ph.D	11/11/15

Abstract

This work investigates the temperature dependence of electron states at the band-edge in ZnO and $Mg_{0.07}Zn_{0.93}O$ thin films.

To investigate the band-edge dynamics, we study in-gap states via temperature dependent absorption spectroscopy in the range 77-527K. The in-gap states at the band-edge were analyzed via the Urbach energy model, where the Urbach energy is a measure of the extent of states into the bandgap. In parallel, we also analyze the temperature dependent Urbach energy via the Wasim model, which separates the relative contributions of defect states and temperature dependent phonon modes to the in-gap states.

It was found that the defect contribution to in-gap states at the band-edge was significantly higher for $Mg_{0.07}Zn_{0.93}O$ than in ZnO. Additionally, the phonon contribution to in-gap states was less in $Mg_{0.07}Zn_{0.93}O$ than in ZnO.

The author gratefully acknowledges the National Science Foundation and the U.S. Department of Energy, Office of Basic Energy Science, Division of Materials Science and Engineering under Grant No. DE-FG02-07ER46386.

Acknowledgements

This space is dedicated to those deserving of recognition for their ongoing advice and support.

My gratitude is offered to Dr. Leah Bergman. Your guidance and insight provided for the duration of this work has helped me to cultivate the skills necessary to make a meaningful contribution to the scientific community.

Thanks go out to my committee members, Dr. Ruprecht Machleidt and Dr. Matthew McCluskey for your efforts and expertise in overseeing this work and my defense.

My colleagues, Dr. Jesse Huso and Dinesh Thapa are deserving of much thanks for providing stimulating discussion and debate in the pursuit of uncovering scientific truth.

My deepest appreciation is extended to Caleb Robinson for his enthusiastic and invigorating discussions. You always seemed to provide the catalyst needed to connect key ideas that extend the breadth and depth of my understanding of the natural sciences at large.

Special thanks are afforded to my parents, Maritta and Jose Luis Canul. Not a day passes that I do not acknowledge the sacrifices you have made that allow me to do the work I am doing today.

Finally, to all my family and friends, you have provided me over the years with nothing but love and support and I am thankful, and so very lucky, to have people like you in my life.

Dedication

To my mother, Maritta Canul, and my father, Jose Luis Canul.

Table of Contents

List of Tables

List of Figures

Introduction

The semiconductor device is of singular import in opening doorways to new technologies that scientists were hardly aware could even exist just a few hundred years ago. The semiconductor could very much be considered the catalyst for launching humanity into the information age and it continues to allow us to push new boundaries in scientific development even today. Semiconductor technology has impacted the advancement of medicine, communications, computing, entertainment, and space exploration, among many others. Perhaps the most obvious impact of semiconductors has been in the field of computing, tracing its roots back through integrated circuits and transistors.

The discovery of the semiconductor dates back to 1874 when the German physicist Karl Braun discovered the asymmetric nature of conduction between metal contacts and semiconductors used in his early experiments on radio.[1] Braun—who built the first cathode-ray tube (CRT) and CRT oscilloscope—discovered that a point-contact semicondutor rectifies alternating current. Around 1898, he invented the technology what would later be known as the Cat's whisker detector, a silicon-based point contact detector, and the first semiconductor electronic device. This detector, further developed by Indian scientist Jagadish Bose and American engineer Greenleaf Pickard at the turn of the 19^{th} century, revolutionized radio- and micro-wave detection. Previous technology based on telegraphy merely detected the presence or absence of the radio signal using dots and dashes. The silicon-crystal detector, largely thanks to its rectification properties, allowed direct conversion to audio.

By 1947 the first transistor, using polycrystalline germanium, was constructed and tested at Bell Telephone Laboratories by William Shockley, John Bardeen, and Walter Brattain after two years and publication of several papers. The group had been assigned to seek a solid-state alternative to vacuum tube amplifiers and succeeded in reducing the technology by one-fiftieth its original size. This technology is widely considered to be the foundation of the information age and has led to the development of almost all modern, compact electronic devices we enjoy today. This was in no small part due to the continued research following its invention.

One of the next great hurdles into the information age became known as the "tyranny of numbers" by those in computer engineering. Engineers were unable to increase the performance of their designs due to the large number of components involved. Every component needed to be wired to most every other component, and were typically strung and soldered by hand. In order to improve performance, more components would be needed, and the outlook showed future designs consisting almost entirely of wiring.

In 1958 Jack Kilby, a then newly employed engineer at Texas Instruments, developed the first integrated circuit from germanium and solved the formidable problem. In a recent interview, Kilby has commented, "the original idea was mine, but what you see today is the work of probably tens of thousands of the world's best engineers." This notion perhaps still rings true today; since the first integrated circuit, circuit design has become orders of magnitude more complex, culminating in the familiar microprocessor of today.

Many hurdles still remain, however, and semiconductors and information processing technology remain at the forefront the research community. Aside from significant reduction in the size of microprocessors, the storage density has also increased dramatically. Information storage and processing is based on the encoding of data by discrete, usually binary, states in some physical system. As the size of microprocessors continues to decrease in parallel with the increase in bit-density, many researchers enter the realm where quantum effects are dominant. In 2009, researchers at Stanford achieved a bit density of 3 Exabytes (1000^6 bits) per square inch, using now-so-called electronic quantum holography technology. Other research groups have pursued biological information storage technologies, including data storage on DNA, which, at the time of this writing holds the record for the highest density storage medium. These novel technologies are yet still in the early research stages and semiconductors still show much promise in the industry.

In addition to its contribution to information technology, semiconductors have significantly impacted light emission and absorption technology. These include but are not limited to solar cells, photo-detectors, light-emitting diodes (LEDs), and laser diodes—all aimed at improving energy management technology worldwide. Of no-

table interest is the development of the first high-brightness blue LED. Despite considerable efforts in the scientific community and in industry, the blue LED remained a challenge for about three decades, but in 1994, was demonstrated by Shuji Nakamura of Nichia Chemicals. The LED was based on InGaN. In parallel, Isamu Akasaki and Hiroshi Amano in Nagoya, Japan, were developing the important GaN nucleation on sapphire substrates and the demonstration of p-type doping of GaN. Nakamura, Akasaki and Amano were all awarded the 2014 Nobel prize in physics for their work. The invention of the blue LED offered a simple and effective way to generate white light. By coating a blue LED with a phosphor material, a portion of the blue light can be converted to green, yellow and red light. This mixture of colored light is perceived by humans as white light and can be used for general illumination. LED lighting technology today reduces electrical power use by approximately 34% over fluorescent lighting.

Other efforts in optical emission and absorption technology have been focused on devices which operate in the ultraviolet (UV) range—between 400 and 100 nm. Although, the majority of the UV spectrum falls outside of the range detectable by humans, UV has a wide application in various fields such as fire detection, UV imaging in astronomy, optical storage and computing, forensics and air and water purification.[2,3] Some specific examples of advantages offered by UV are: increased storage density in optical storage media and increased security of short-range communications.[4–6] through significant reduction in "read" laser diameter due to strong atmospheric scattering

Despite advantages of UV-based technology, there are still few true-UV solid state sources and detectors available today. Frequency doubling technology can generate UV from longer wavelength sources, but such processes are inherently less efficient than a source that directly emits UV. Furthermore, the vast majority of true-UV sources and detectors consist of bulky and fragile lamps and filters, which, among other things, prohibit the mobility of such technology. Moreover, solid states devices for the UV are uncommon and have only recently become available for purchase in the form of LEDs. However, poor efficiency and wavelength selectivity leave much room for improvement in the technology.

In efforts to improve on solid state UV emitting technology, the semiconductor Zinc Oxide (ZnO) has gained considerable interest in the research community largely thanks to its non-toxic nature and its efficient operation at room-temperature.[7] Another interesting property of ZnO is its transparency to visible light, which may lead to potential applications in transparent Ohmic contacts for light emitters, solar cells, and transparent thin-film transistors.[8]

Research focusing on ZnO predates the invention of the transistor and dates back to 1935, when C. W. Bunn published studies of its lattice parameters settling a disagreement between the parameters determined by X-ray and electron-diffraction.[9] Bunn's experiments involved the former using Zinc-oxide smoke made by the combustion of pure granulated zinc. Following this, the optical properties of ZnO were studied in detail by Mollwo in 1959 and the vibrational properties were studied via Raman scattering by Damen, et al in 1966.[10,11] A year later, LEDs were demonstrated by Drapak, wherein Cu_2O was used as the p-type material.[12] P-n junctions were then accomplished in 1975 by Tsurkan, et al. via ZnO/ZnTe.[13] Beginning a couple decades later, numerous controversial reports of p-type ZnO have been reported, beginning with Minegishi's paper in 1997. Intrinsic ZnO is n-type for reasons that are still largely unknown to researchers, and synthesizing high concentration p-type ZnO remains a major hurdle in advancing the technology today.[14]

The study of doping and bandgap engineering in ZnO has also received much attention in recent decades. Bandgap engineering forms the basis for many electrical and optical semiconductor based-devices. ZnO can be alloyed with Mg and Be for "widening" the bandgap and alloyed with Cd for "closing" the bandgap. In addition to altering the energy gap, bandgap engineering is accompanied by a potential change in a host of other mechanical and optical properties of the main member in the alloy, depending on percentage composition.[15,16] No doubt, synthesizing p-type ZnO remains a primary objective of doping.[17–21]

This work presents research on ZnO polycrystalline thin films and its alloy MgZnO, and looks specifically at optical transitions near the band-edge as a function of temperature. To this end we first explore the nature of the solid state as it pertains to semiconductors, followed by expanding on bandgap engineering in Chapter 1, and

the synthesis of semiconductors in Chapter 2. Following this is a brief introduction to the interaction of radiation with matter is given in Chapter 3. In Chapter 4,we move on to treat spectroscopic methods used in this work to extract information about the semiconductor samples, specifically, UV-visible absorption spectroscopy. In Chapter 5, our attention then turns toward a presentation of experimental results followed by a discussion of experimental analysis including the application of various models found throughout literature. In the 6th and final chapter, the relevance and impact of this study is discussed and concludes in potential future work.

REFERENCES

[1] F. Braun, Annalen der Physik und Chemie **229**, 556 (1875).

[2] S. Kj and W. Rb, Laboratory practice **22**, 103 (1973).

[3] A. N. Cox, *Allen's astrophysical quantities* (2000).

[4] J. Huso, Ph.D. Thesis , 292 (2012).

[5] G. Chen, F. Abou-Galala, Z. Xu, and B. M. Sadler, Optics Express **16**, 15059 (2008).

[6] B. Charles, B. Hughes, A. Erickson, J. Wilkins, and E. A. Teppo, in *OE/LASE'94* (International Society for Optics and Photonics, 1994) pp. 79–86.

[7] P. A. Rodnyi and I. V. Khodyuk, Optics and Spectroscopy **111**, 776 (2011).

[8] K. Nomura, H. Ohta, K. Ueda, T. Kamiya, M. Hirano, and H. Hosono, Science **300**, 1269 (2003).

[9] C. W. Bunn, Proceedings of the Physical Society **47**, 835 (1935).

[10] G. Heiland, E. Mollwo, and F. StÃűckmann, in *Solid State Physics*, Vol. 8, edited by F. S. a. D. Turnbull (Academic Press, 1959) pp. 191–323.

[11] T. C. Damen, S. P. S. Porto, and B. Tell, Physical Review **142**, 570 (1966).

[12] I. T. Drapak, Semiconductors 2 **624** (1968).

[13] A. E. Tsurkan, N. D. Fedotova, L. V. Kicherman, and P. G. Pas'ko, (1975).

[14] K. Minegishi, Y. Koiwai, Y. Kikuchi, K. Yano, M. Kasuga, and A. Shimizu, Japanese Journal of Applied Physics **36**, L1453 (1997).

[15] A. Ohtomo, M. Kawasaki, T. Koida, K. Masubuchi, H. Koinuma, Y. Sakurai, Y. Yoshida, T. Yasuda, and Y. Segawa, Applied Physics Letters **72**, 2466 (1998).

[16] X. D. Zhang, M. L. Guo, W. X. Li, and C. L. Liu, Journal of Applied Physics **103**, 063721 (2008), arXiv: 1210.0163.

[17] M. Joseph, H. Tabata, and T. Kawai, Japanese Journal of Applied Physics **38**, L1205 (1999).

[18] M. Joseph, H. Tabata, H. Saeki, K. Ueda, and T. Kawai, Physica B: Condensed Matter Proceedings of Yanada Conference LIV. The 9th International Conference on Shallow-Level Centers in Semiconductors, **302-303**, 140 (2001).

[19] Y. R. Ryu, S. Zhu, D. C. Look, J. M. Wrobel, H. M. Jeong, and H. W. White, Journal of Crystal Growth **216**, 330 (2000).

[20] T. Yamamoto and H. Katayama-Yoshida, Japanese Journal of Applied Physics **38**, L166 (1999).

[21] C. Wang, Z. Ji, K. Liu, Y. Xiang, and Z. Ye, Journal of Crystal Growth **259**, 279 (2003).

CHAPTER 1

Semiconductors & Bandgap Engineering

Introduction — The bandgap is perhaps the single most useful property of semiconductor materials. The bandgap allows the semiconductor to operate as an energetic switch, facilitating the flow of energy into (or out of) the semiconductor at pre-determined values. The energy of the bandgap is dependent on the chemical interactions between sub-unit atoms in the solid; therefore, we can engineer bandgaps by altering the semiconductor at the atomic level.

1.1 ENERGY STATES

The behavior of semiconductors is understood by considering what happens when similar atoms are brought together to form a solid. As the interatomic distance of a solid crystal is reduced, wave functions which constrain the energetic state of the electrons begin to overlap. In accommodating Pauli's exclusion principle, all spin-paired electrons in the crystal acquire energies slightly different from other spin-pairs and from the energy possessed in an isolated atom. The collection of adjusted electron energy states is described by a quasi-continuous band of energy levels. Fig. 1.1 shows the distribution of states as a function of the interatomic distance or lattice constant.

As shown in Figure 1.1, further reducing atomic separation of the crystal lattice does not reduce the cohesive energy of the crystal indefinitely, but there exists an ideal separation which yields the lowest energy state. The energy gained by arranging the atoms in a crystalline state is maximum for some finite lattice constant(s). For example, carbon crystal structures corresponding to a lattice constant at the energy minimum shown in the figure produces the material diamond.

In the model shown, the energy band formed by overlapping $2p$ orbitals merge with that formed by interfering $2s$ orbitals, thus leading to a distinct upper and lower

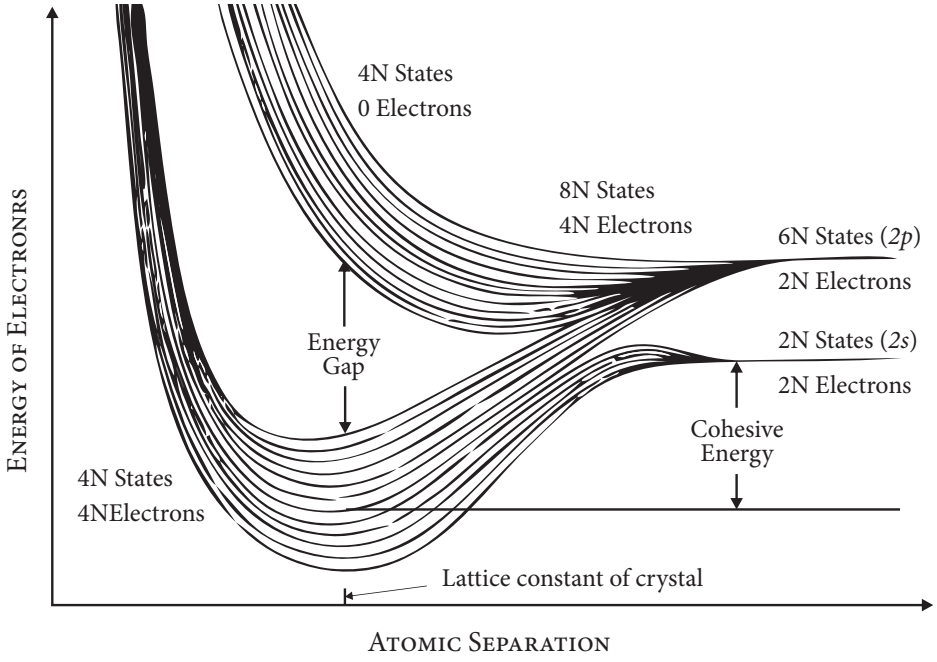

FIGURE 1.1: *Energy bands of allowed levels in diamond as a function of lattice constant.*[1]

band. The split leads to a mixture of s and p orbitals, or hybridized orbital, which redistributes all electrons to fill the lower band. The lower energy band is called the valence band and contains as many states as electrons.

When a band is filled, and all possible electron states are occupied, the solid cannot carry a current. However, the upper band, or conduction band, contains no electrons, so an electron must assume energies available here in order to travel through the crystal and produce a current. Furthermore, the transition from a valence to conduction state will not take place in the absence of the energy described by the bandgap.

1.2 CLASSIFICATION OF SOLIDS

Solids are classified as conductors (or metals), semiconductors, or insulators depending on the range (or presence) of the energy gap and the relative availability of conduction electrons.

In semiconductors, the energy gap may extend over a range of about three electron-volts (eV) and the number of electrons per cubic centimeter in the upper band, having enough energy for mobility, is less than 10^{20} cm^{-3}. In a conductor, the upper band is partially filled and is populated on the order of about 10^{23} electrons per cubic cm at energies significantly higher than that of the maximum gap energy. Lastly, insulators are characterized as having a large energy gap, greater than 3 eV, and negligible electron concentration at energies in the upper band. The energy diagram model, shown in Fig. 1.2, highlights the differences among the three primary classes of solids.

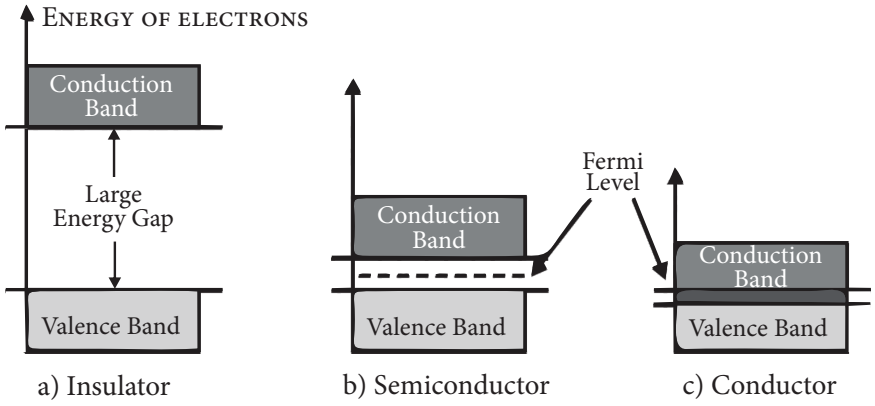

FIGURE 1.2: *Solids are generally classified as conductors, semiconductors or insulators depending on the range of the energy gap and the relative availability of conduction electrons.*[2]

1.3 DENSITY OF ELECTRON STATES

The total density of states up to some energy E is derived from the volume of momentum space between two constant energy surfaces. A single spin state occupies a

given volume in momentum space and there are two states per energy level (Pauli). In addition, each (spatially local) potential valley contributes its own set of states, so each energy level may consist of states from several valleys. The resulting variation of the density of states in the conduction and valence band near the energy gap is shown in Figure 1.3.

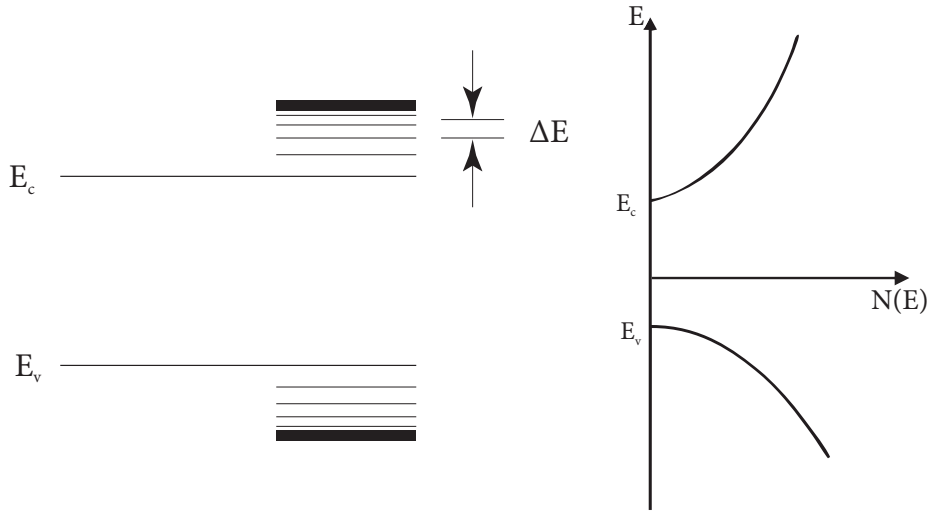

FIGURE 1.3: *The variation of the density of states near the energy gap.*

The above model is given for an ideal semiconductor.

1.4 CARRIER CONCENTRATION

So far the treatment of the motion of electrons in a semiconductor has been focused on energy and momentum constraints on the electron. However, electron *states* may or may not be occupied. Thus, the Fermi-Dirac function statistically models how likely energy states are to be occupied at a given temperature. The function is given as follows:

$$f(E) = \frac{1}{e^{\frac{(E-E_F)}{kT}} + 1} \tag{1.1}$$

Figure 1.4 shows the Fermi-Dirac function at two temperatures. The Fermi level is the energy level within the gap at which the probability of finding an electron is 1/2. Furthermore, the total likelihood of an electron being in any of the allowed states, i.e. the density of electrons in any state, is simply the product of the density of states and the Fermi-Dirac distribution function.

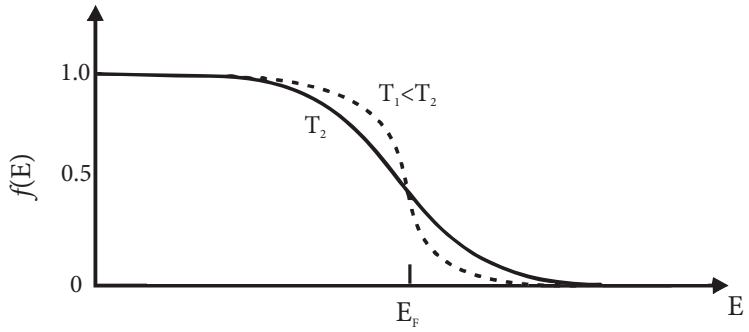

FIGURE 1.4: *The Fermi-Dirac function at two temperatures. The products of the density of states and the Fermi-Dirac distribution determines the electron concentration at various energies.*

Most electrons in a semiconductor are in the valence band leading to no free electrons to conduct current. Strictly speaking, this is true only at absolute zero temperature. At any other temperature a small portion of electrons will acquire sufficient thermal energy to become conduction electrons. At room temperature, the density of electrons and holes is very small given that thermal energy at room temperature, given by kT, is 26 meV. In practice, it is possible to significantly increase the number of conduction electrons (or holes) in a semiconductor by introducing suitable impurity atoms into a lattice structure—a process commonly referred to as doping. The following sections expand on this topic and the remainder of this work focuses on "large scale" doping or alloying.

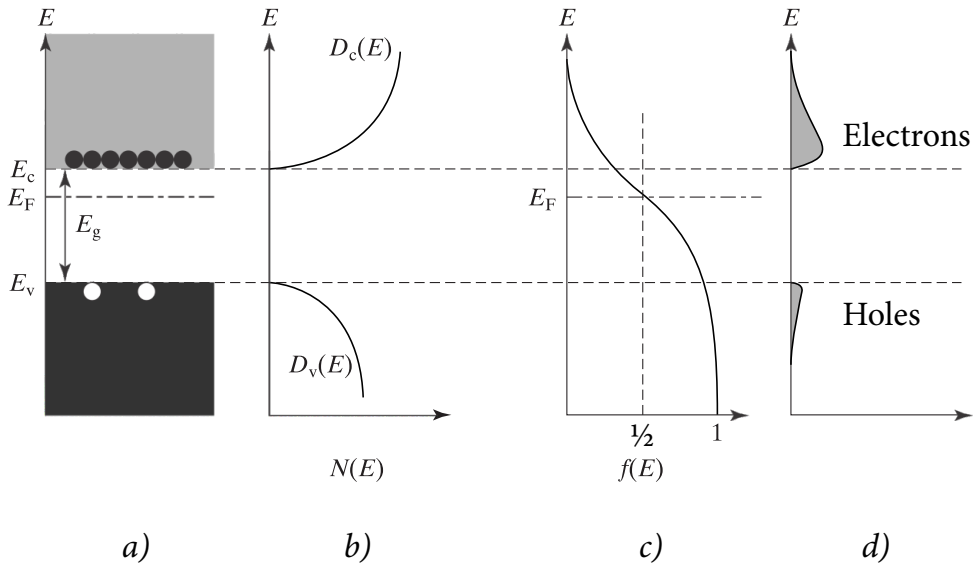

FIGURE 1.5: *(a) Schematic band diagram, (b) density of states, (c) Fermi-Dirac distribution and (c) carrier distributions versus energy.*[3]

1.5 ALLOYING—ZNO & MGO

Currently in the field of bandgap engineering, there remains a limited number of accessible bandgap energy ranges. If the need arises for a device that operates in a particular energy range that is not available naturally, the appropriate materials must be created. One method of bandgap engineering focuses on introducing a substitutional impurity (or multiple impurities) to create a semiconductor alloy, which, in essence, is a solid solution of multiple materials. This work focuses on the extrinsic semiconductor ZnO and its alloy $Mg_xZn_{1-x}O$. In the $Mg_xZn_{1-x}O$ alloy system, Zn lattice points are substituted with Mg atoms to create the ternary compound.

To understand the interaction between alloyed semiconductors, we must first be familiar with the component parts. ZnO is a semiconductor with a wurtzite crystal structure, a bandgap of approximately 3.3 meV and an exciton binding energy of approximately 60 meV. MgO, more an insulator, has a cubic crystal structure, a bandgap of approximately 7.8 eV and an exciton binding energy of 100 meV.[4]

Substituting Mg for Zn in the ZnO lattice changes the optical properties of the lattice as a whole. The changes are largely based on the ratio of electronegativities of Mg to Zn, the ratios of their covalent radii, and also on the ratio of their mass. The ratio of the mass of Mg to Zn is considered to be ≈ 1, and the two atoms have comparable covalent radii, although Mg is slightly larger.

As shown in Tab. 1.1, the electronegativity of Mg is less than that of Zn. The ratio of electronegativities of O to Mg is ≈ 2.63. Therefore the electron density of MgO is located around O and MgO is said to be ionically bonded. In the case of ZnO, the ratio of electronegativities of O to Zn is ≈ 2.08—less than that of 2.63 in MgO. Therefore the electron density accumulates between Zn and O more equally in a semi-ionic-covalent bond.

MgO crystal structures exist in the rocksalt cubic phase, whereas ZnO crystal structures exist in the hexagonal wurtzite phase as shown in Fig 1.6.[5] The mismatch

in crystal structures of the alloy end-members gives $Mg_xZn_{1-x}O$ varying crystal structure depending on Mg concentration. Additionally, solubility plays a key role in governing the properties of this alloy.

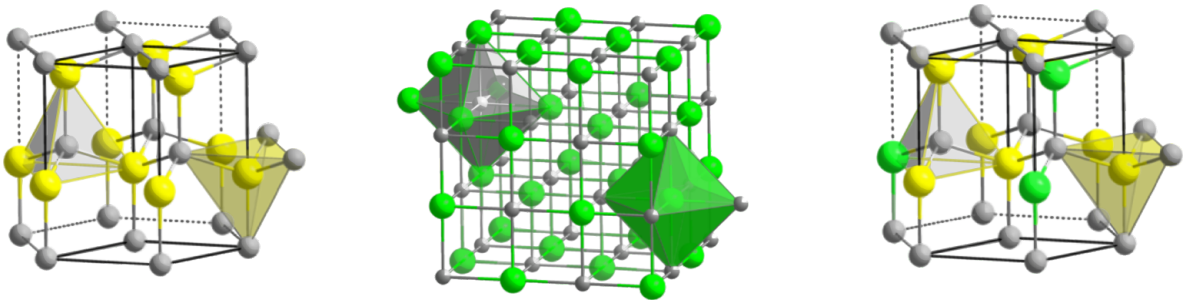

FIGURE 1.6: *(a) The wurtzite hexagonal crystal structure of ZnO. (b) The rocksalt cubic crystal structure of MgO. (c) At low concentrations, $Mg_xZn_{1-x}O$ retains a wurtzite structure.*

1.5.1 *Solubility of Crystal Structures*

The extent of the solubility of a substitutional impurity in a semiconductor is measured by the saturation concentration. Saturation concentration in $Mg_xZn_{1-x}O$ is the point at which the wurtzite-type alloy can dissolve no more Mg without precipitating cubic-phase MgO. This results in a mixed-phase wurtzite-cubic material and is known as phase segregation. Saturation in $Mg_xZn_{1-x}O$ has been shown to occur at about 40% Mg. This mismatch in crystal structure between ZnO and MgO leads to a limitation in solubility on both ends of the alloy composition spectrum, that is, Mg-doped ZnO and Zn-doped MgO, at equilibrium.[1] Accordingly, extremely high concentrations of Mg lead to cubic structure $Mg_xZn_{1-x}O$.[6]

[1] Equilibrium refers to a state in which the relative phase composition is stable and the concentration of atoms in any given phase remains constant in time.

TABLE 1.1: *Material properties of MgO and ZnO and constituent atoms, Mg, Zn & O.*

Compound	**Structure**	**Lattice Constants (Å)**	**Bandgap *(eV)***
MgO	Rocksalt Cubic	a = 4.2	7.8
ZnO	Hexagonal Wurtzite	a = 3.2 c = 5.2	3.4
Atom	**Covalent Radius (Å)**	**Electronegativity†**	**Oxidation States**
Mg	1.36	1.31	$+2$
Zn	1.25	1.65	$+2$
O	0.73	3.44	$-2, -1$

† Pauling's

After obtaining the ternary compound $Mg_xZn_{1-x}O$, the bandgap settles somewhere between the two bandgaps of the end-members, based on composition of the compound, and lies between 3.3–7.8 eV. The value of the energy gap of a ternary semiconductor alloy is determined by the following equation:[7]

$$E_{g,MgZnO}(x) = (1-x)E_{g,ZnO} + xE_{g,MgO} - bx(1-x) \tag{1.2}$$

where x is the composition fraction, E are the respective bandgap energies, and b is the bowing parameter. The quantity b incorporates the mismatch in electronegativities and covalent radii between the substituting atomic species in the determination of the alloy bandgap.[8,9] Thus, the bowing parameter describes the deviation from linear behavior of the bandgap with composition in the alloy system.

When $b = 0$, the bandgap of the alloy changes linearly with respect to the relative composition of the two binary compounds. When $b > 0$, the behavior of the resultant bandgap exhibits a bowing effect, which makes it possible to create an alloy with a bandgap lower than that of either end binaries. One of the first reports of the synthesis of $Mg_xZn_{1-x}O$ with a Mg content of up to 33% was by Ohtomo et al.[10] by pulsed laser deposition (PLD). Ohtomo found a linear increase in the bandgap with composition up to 4.15 eV for $0 < x < 0.36$.

Bandgap bowing in $Mg_xZn_{1-x}O$ is therefore not an issue in practice, and this ternary system is created to increase the bandgap in ZnO.[11] Fig. 1.7 shows that bandgap engineering of ZnO with Mg achieves a wide range of bandgap energies from UV well into the visible.

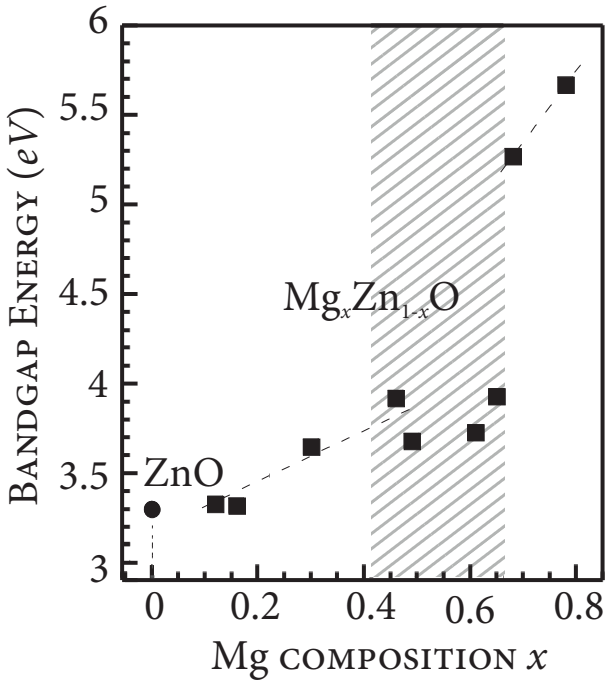

Figure 1.7: *Bandgap engineering of ZnO can achieve a wide range from UV into the visible. Squares represent the bandgap energy of $Mg_xZn_{1-x}O$. The shadowed area indicates the phase segregation region where cubic and wurtzite crystal structures coexist. Figure adapted from Hui (2014).*[12]

The $Mg_xZn_{1-x}O$ alloy investigated in this work consists of 7% Mg by composition, confirmed by EDS, which corresponds to a wurtzite type alloy with a bandgap slightly wider than that of ZnO.

1.6 EFFECTS OF ALLOYING ON THE BAND-EDGE

1.6.1 *Tailing*

While alloying offers many benefits to semiconductor technology, impurities form additional energy levels of their own and cause extrinsic band edges to be distorted via Coulomb interaction. This distortion leads to the formation of "tails" extending into the energy gap as a result of the increase in band-edge energy levels. The nature and source of tailing-states at the band-edge in semiconductors, and the Urbach model of tailing is the focus of this work and will be treated in further rigor in following sections.

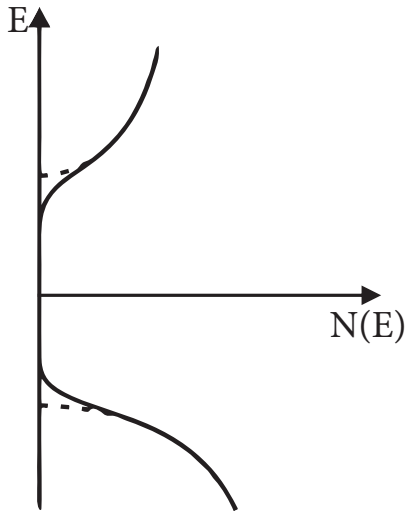

FIGURE 1.8: *Tails within the bandgap describe an exponential decay of available states approaching the energy gap from either the CBM, or the VBM. This is due to the presence of impurities which distort extrinsic band edges (shown by the dotted lines) by Coulomb interaction.*

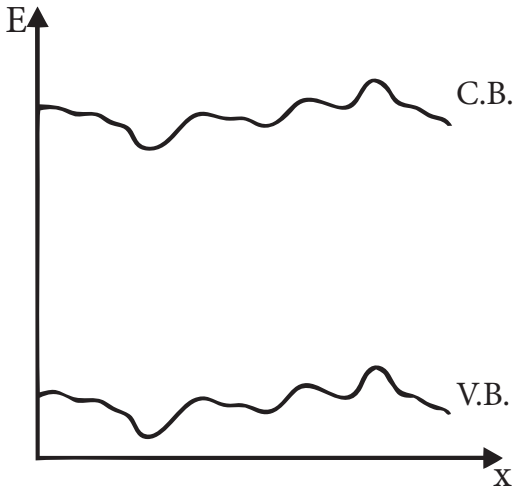

FIGURE 1.9: *Inhomogeneously distributed impurities perturb the band edges by Coulomb interaction.*[1]

1.6.2 *Defects*

In addition to impurity-band formation and tailing, other mechanical changes in doped semiconductors may come about.

Since a substitutional impurity would normally possess a covalent radius that is larger or smaller than the host atom, mechanical strain is introduced in the lattice, and can be either compressive or dilatational. An interstitial can also introduce a compressional strain whereas a vacancy can introduce a dilational strain. Compression and dilation can increase and reduce the energy gap, respectively, due the presence of additional atomic nuclei, or lack thereof. This effect is directly linked to the band edge perturbation previously discussed. Crystallographic defects known as dislocations also contribute to irregularities within a crystal. Dislocations occur at the edge of an extra plane of atoms and are characterized by the mismatch between planes of atoms, especially at grain boundaries. Dislocations produce both compressional and dilational strains which also perturb the band edges.

More information on structural defects and their effects on the band-edge is given in Sec. 4.6.

Conclusion — We have seen in this chapter that altering the intrinsic nature of semiconductors may result in potentially changing any number of its electrical, optical, and mechanical properties. In $Mg_xZn_{1-x}O$ we widen the bandgap of ZnO but expect to see an increased presence of tailing states at the band-edge corresponding, in part, to defects intrinsic in the nature of alloying.

REFERENCES

[1] J. I. Pankove, *Optical processes in semiconductors* (Prentice-Hall, Englewood Cliffs, NJ, 1971).

[2] C. Kittel, *Introduction to Solid State Physics*, 8th ed. (Wiley, Hoboken, NJ, 2004).

[3] C. C. Hu, *Modern Semiconductor Devices for Integrated Circuits*, 1st ed. (Prentice Hall, Upper Saddle River, N.J, 2009).

[4] R. C. Whited, C. J. Flaten, and W. C. Walker, Solid State Communications **13**, 1903 (1973).

[5] A. F. Wells, *Structural Inorganic Chemistry*, 5th ed. (Oxford University Press, Oxford Oxfordshire : New York, 1984).

[6] J. L. Morrison, J. Huso, H. Hoeck, E. Casey, J. Mitchell, L. Bergman, and M. G. Norton, Journal of Applied Physics **104**, 123519 (2008).

[7] J. A. Van Vechten and T. K. Bergstresser, Physical Review B **1**, 3351 (1970).

[8] M. Ferhat, physica status solidi (b) **241**, R38 (2004).

[9] N. Tit, I. M. Obaidat, and H. Alawadhi, Journal of Physics. Condensed Matter: An Institute of Physics Journal **21**, 075802 (2009).

[10] A. Ohtomo, M. Kawasaki, T. Koida, K. Masubuchi, H. Koinuma, Y. Sakurai, Y. Yoshida, T. Yasuda, and Y. Segawa, Applied Physics Letters **72**, 2466 (1998).

[11] A. Zeuner, H. Alves, D. M. Hofmann, B. K. Meyer, M. Heuken, J. BlÃd'sing, and A. Krost, Applied Physics Letters **80**, 2078 (2002).

[12] H. Che, *Band gaps by design : Tailoring ZnO based semiconductor alloy films*, Ph.D. thesis (2014).

CHAPTER 2

Thin Film Synthesis

Introduction — In this chapter, we outline the growth approach used in this work. We specifically discuss the measures implemented in order to ensure the repeatability of growth experiments in addition to ensuring optimum sample quality. The ZnO and $Mg_{0.07}Zn_{0.93}O$ thin films studied in this work were grown via DC magnetron sputtering using custom sputtering targets.

2.1 PHYSICAL VAPOR DEPOSITION & SPUTTERING

Physical vapor deposition methods comprise techniques such as RF (Radio Frequency) and DC (Direct Current) magnetron sputtering, the latter being used in this work. Aside from common use in the semiconductor industry, sputter deposition has found utility in industrial tool bit coating applications and optical coating for glass and storage media and has been used as long ago as 1877 to coat mirrors.[1–3] The phenomenon of sputtering was first described over 150 years ago by William Robert Grove in 1852 and independently by Julius Plücker in 1858 who reported vaporization and film formation of metal films by sputtering.[4,5]

Formerly known as cathode disintegration, sputtering, as its dated name implies, fundamentally involves the disintegration of a material and subsequent deposition of this material onto a substrate.[6] The process involves several components including electrodes, sputtering targets or coating material, sputtering gases (that may be inert or reactive) and substrates.

The working gas is introduced into the sputtering chamber, initially placed under vacuum. This gas is then ionized in the chamber via an applied electric field. A cascade of positively charged ions is then initiated in the plasma; these ions are accelerated toward the anodic sputtering target and collide with target surface molecules.

This bombardment results in molecular ejection via the transfer of momentum. Upon displacement, the displaced target material falls and deposits uniformly onto the substrate aligned below. Generally, the dislodged target material is electrically neutral and is able to pass through the applied electric field uninhibited. This process is illustrated in Fig. 2.1.

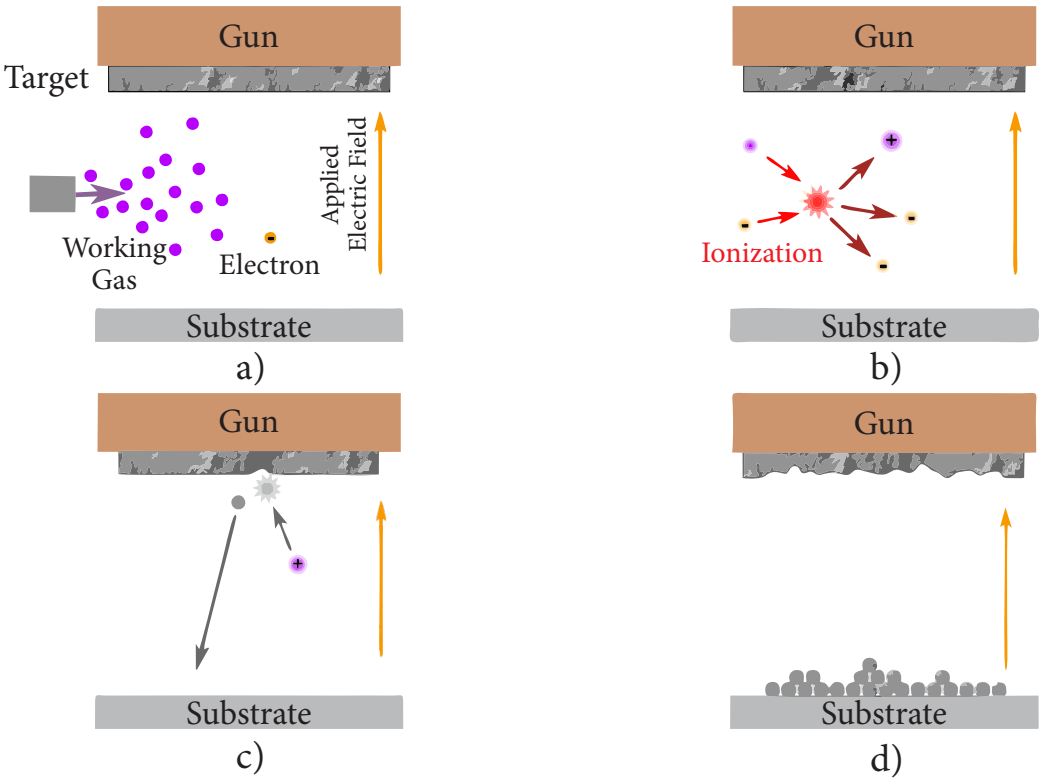

FIGURE 2.1: *A schematic illustrating the process of DC sputtering. (a) The chamber is filled with the working gas and electrons are accelerated by the applied electric field. (b) The electron collides with a working gas atom—an ion and more electrons are generated. (c) The ion is accelerated toward and bombard the target, ejecting a small portion of the target. The ejected material travels and deposits onto the substrate. (d) This process is repeated over time until the substrate is coated with a thing layer of the target material.*

Reactive sputtering occurs when the sputtered material undergoes a reaction with a reactive gas on the path from target to substrate. In this work, Zn and Zn–Mg sputtering targets are bombarded by Argon ions which act as the inert gas and Oxygen gas acts as the reactive agent. This combination results in the deposition of ZnO and

$Mg_{0.07}Zn_{0.93}O$ type thin film alloys, respectively. Sputtering, in light of the many parameters present, provide a great degree of control over the microstructure and growth of thin films.

These parameters include, but are not limited to, those mentioned previously—target material, working and reactive gases—in addition to the flow rate of both gasses, chamber temperature and pressure, target power source, sputtering power, magnetron configuration of the sputtering gun, and magnetic shielding of the substrate. Each of the aforementioned parameters and their effect on thin film growth will be discussed herein.

The average number of target atoms released per incident ion is known as the sputtering yield. Simply put, this yield is a function of both ion and target atom(s) masses, ion incident angle and energy, and the surface binding energy of atoms on the target surface.[7] In addition to these considerations, in crystalline targets, the orientation of crystal axes can be modified with respect to the surface orientation, thereby affecting the surface binding energy, albeit usually negligibly so.

2.2 SPUTTERING GASES

Working and reactive gases play a crucial role in controlling thin-film properties. As mentioned previously, the working gas atom transfers momentum to the target atom and thus, if both species possess a mass of similar order, this transfer takes place most efficiently. When working with gases, pressure becomes a significant variable to consider. The chamber pressure throughout sputtering comprises a preliminary base pressure, P_{base}, the plasma strike pressure, P_{strike}, initial working gas pressure, P_{Ar}, and a working pressure, P_{total}. *In this work, Argon is used as the working gas.*

The chamber is first pumped down to its minimum base pressure before growth. Argon is then introduced into the chamber to strike the plasma. Following this, the

Argon flow is adjusted and pressure is lowered in preparation for growing. If a reactive gas, P_{reactive} is required, it is now introduced to achieve the total, or working, pressure needed for growing.

Dalton's law of partial pressure states that the total pressuring of the mixture of non-reactive gases is equal to the sum of the partial pressure of individual gases. Therefore, the total pressure in the sputtering chamber during the sputtering process is given by the following:

$$P_{\text{total}} = P_{\text{base}} + P_{\text{working}} + P_{\text{reactive}} \tag{2.1}$$

Sputtering power should ensure that ions posses enough momentum for collision, while partial pressures and flow rate ideally ensure the minimization of mean free path, allowing Ar ions to travel to the target efficiently.

In general there is an optimum total operating pressure to maximize deposition rate. The trick to picking an optimum pressure is a compromise in the interplay between increasing the number of Ar ions available for sputtering and increasing the scattering events (reduced mean free path) between Ar ions and neutral Ar atoms.

2.3 ARC SUPPRESSION

When using a conductive target, a DC power source is preferable because it increases the rate of sputtering and in turn reduces total sputtering time. DC power sources, however, are more prone to arcing, which is a source of several unwanted, and sometimes also dangerous, issues in sputtering. When the uniform glow of a plasma develops intense, localized concentrations of energy, usually due to the formation of insulating regions, arcing results—a phenomenon similar to lightning.[8] The intense energy evolved near arcing sites can result in explosive, and potentially harmful, ejection of macro-particles. There are several methods to combat arcing when sputtering

in the DC regime. Reverse-voltage pulsing has been shown to dramatically reduce arcing, while other electronics, equipped for arc detection and suppression, attenuate this phenomenon, but unfortunately do not prevent it completely.[9] Sputtering with highly pure targets is required since small impurities on the surface of the target can lead to arcing.

When using an insulating target, consistent bombardment of the insulator results in significant build-up of positive charge, which in turn repels incoming ions of the working gas. As this phenomenon continues over time, an increased sputtering power is required to maintain sputtering rate, in some cases up to 10^{12} volts. In many instances sputtering rate is dramatically reduced and possibly halted altogether. One method of circumventing this problem is in using RF sputtering.

In RF sputtering, the polarity of the applied electric field is alternated by driving the sputtering gun at a particular frequency, unlike the fixed voltage in DC sputtering. For the first half of the alternating cycle, positively charged ions are driven toward the target and electrons are driven toward the substrate. This portion of the cycle is similar to that of DC sputtering and thus the target begins to be affected by charging. However, the alternating cycle reverses the polarity of the applied field and drives electrons back toward the target, neutralizing it. This cycle of brief charging and subsequent neutralization significantly reduces the occurrence of ion repulsion, unfortunately, at the cost of sputtering rate—a direct result of only sputtering over half-cycles.

2.4 SUBSTRATES

The substrate chosen for sputtering has the ability to affect the structural properties of deposited thin films. Generally, growing on material that has a similar if not the same lattice parameters (and crystal orientation) as the film is beneficial. In cases where

lattice parameters are not similar enough between substrate and alloy, a buffer layer could first be introduced which serves as an average to "bridge" lattice parameters. Differently cut substrates will have different lattice parameters, namely, z, x, y, m and n-cut.

Potential interference of substrates with spectroscopic techniques also bears considering. For example, when a chemical element is common to both substrate and sample, EDS alloy compositional readings may detect elemental traces from the substrate. Another example of possible instrumental interference is a substrate with high potential for photoluminescence, which can interfere with UV-Photoluminescence measurements.

If crystal orientation is not a concern, i.e. in polycrystalline materials, mechanical properties of the substrate come into consideration. Quartz and Sapphire may be chosen for their high melting point, transparency to UV or relative durability while fluorinated ethylene propylene (FEP) may be chosen for its flexibility.

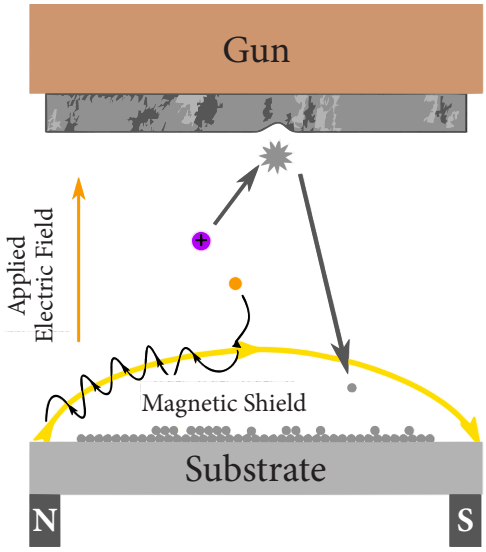

FIGURE 2.2: *During sputtering, a substrate is magnetically shielded. A magnetic field (yellow) is created directly beneath the substrate and the resulting field captures charged particles, particularly electrons, preventing them from damaging the substrate and sputtered coating.*

2.5 MAGNETIC SHIELDING

Due to the high energy environment of the sputtering chamber, safety measures must be implemented to protect substrates and deposited material. As an example of why these measures are sometimes necessary, consider the alternating polarity of the applied electric field in RF sputtering. This reversed polarity not only reduces charge buildup on the target, but redirects ions from the working gas toward the substrates, potentially reversing deposition achieved heretofore, if not damaging the substrates completely. Polymer substrates are notably susceptible to damage in this fashion. Upon collision with the substrate, even in DC sputtering, the mean free path of electrons is so confined to the thin surface layer that all the kinetic energy is directed into virtually boiling this layer of the substrate. To combat collisions of charged particles with the substrate, we introduce magnetic shielding based on the Lorentz Force Law:

$$\vec{F} = q(\vec{E} + \vec{v} \times \vec{B}) \tag{2.2}$$

where q represents the charge of the particle, E is the electric field, v is the velocity of the charged particle and B is the magnetic field.

As seen in the Fig. 2.2, a magnet placed beneath the substrates generates the field that protects the substrate from damage by electrons and ions, in both DC and RF sputtering, but allow through sputtered material.

2.6 MAGNETRON SPUTTERING

Further adjustments may be implemented to the sputtering system in order to increase the sputtering rate. "Surface magnetron" sputtering configurations were introduced in the 1960s and early 1970s after the effects of a magnetic field on the trajectories of electrons had been realized.[10] These magnetron sources use a magnetic field that

loop in and out of the target surface in a closed "racetrack" pattern as shown in Fig. 2.6. Electrons are then confined to this "racetrack" thereby resulting in high density plasma near the target surface. This high density plasma area contains more ions and in turn contributes to the increase in sputtering rate. Magnetron configurations can be utilized in conjunction with DC or RF sputtering.

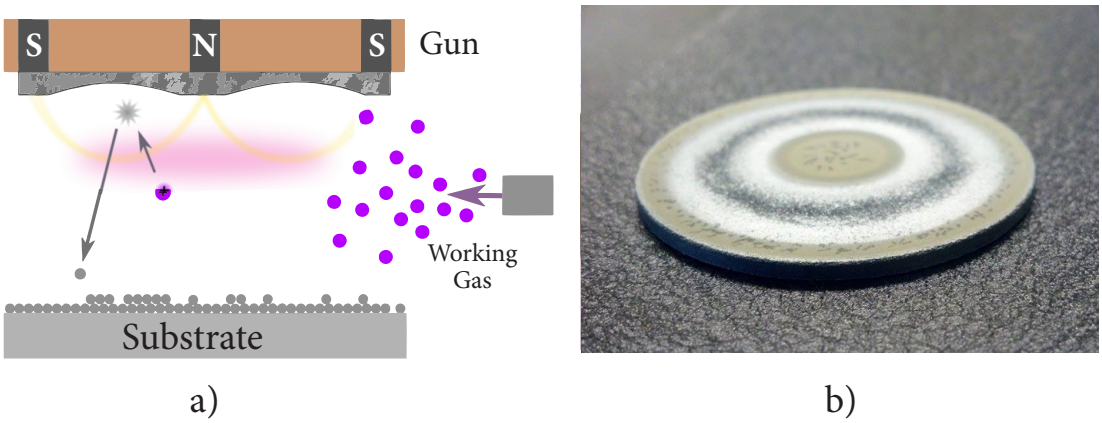

FIGURE 2.3: *(a)*A cross section view of the magnetron configuration used in this work. *(b)* A sputtered Zn-Mg target. The racetrack shaped pattern on the target suggests an area with enhanced sputtering rate by confining electrons within a certain region via the magnetic field.

2.7 SPUTTERING SYSTEM IN THIS WORK

The sputtering chamber utilized in this work is custom built. The following paragraphs outline some of the system's components and capabilities.

The sputtering chamber uses a Varian V200 molecular Turbo pump coupled with a Welch model 1402 DuoSeal belt-drive mechanical roughing pump and interlocking system that monitors flow. The chamber is vacuum sealed using Viton elastomer flanges and copper conflate-style flanges. Pressure in the system is determined via a triple-gauge configuration. A Duniway Convection gauge measures in the range

1000–10^{-4} *Torr*, a capacitive gauge measures in the range 100–10^{-4} *Torr*, and a Bayard-Alpart style hot cathode ion gauge measures in the range 10^{-3}–10^{-10} *Torr*. The preceding configuration takes the chamber to a well-monitored 2.6×10^{-6} *Torr*. Despite the mixture of multiple gases in the chamber, the capacitive gauge monitors pressure during growth independent of chamber gas composition. This feature is most useful during reactive sputtering.

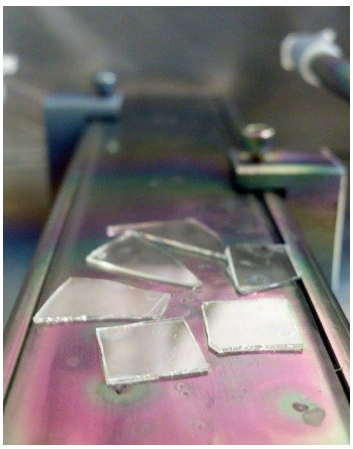

FIGURE 2.4: *A photograph of sputtered $Mg_{0.07}Zn_{0.93}O$ samples studied in this work. The samples were grown on Quartz and Sapphire substrates.*

The sputtering system utilizes a double-gun configuration capable of dual-target sputtering. However, only single-target sputtering is used in this work via a water cooled ST20 magnetron sputtering gun from AJA International. This gun is only compatible with 2–inch diameter disk targets. Flow of both working and reactive gasses, Argon and Oxygen, is monitored independently upstream from the sputtering chamber. Flow is regulated by MKS Type P4B digital Mass Flow Controllers (MFC) based on differential heat transfer between temperature-sensing heater elements attached to the exterior of the sensing tube. Real-time gas flow control is achieved through a computer-based flow control application. The MFC and flow control application work in conjunction to gauge flow with a resolution of 0.07 standard cubic centimeters per minute (*sccm*) and an accuracy of approximately $\pm 1\%$.

FIGURE 2.5: *A photograph of the sputtering system used in this work. On the right is the growth chamber, beneath which can be seen the turbo molecular vacuum pump backed by the mechanical roughing pump. On the left is an equipment rack with all accompanying control electronics and power sources.*

By closely monitoring the introduction of each gas to the sputtering system and the contribution of each gas to Dalton's law of pressure we insure the repeatability of experiments with reasonable accuracy.

2.8 TARGETS

The targets used in this work were custom-made Zn–Mg and Zn–metal targets. The Zn–Mg targets were made by mixing Mg and Zn metal powders in desired ratios followed by pressing the mixture into a 2–inch die by a Carver hydraulic press, at 50,000 *lbs* for over 24 hours. The Mg and Zn metal powders were purchased from Alfa Aesar and are of 99.8% and 99.9% purity, respectively.

The most significant advantage of pressed metal targets lies in the freedom of controlling the Zn-Mg ratio, as compared to the limited choices of commercially available ones. However, pressed metal targets cannot endure high input power due to its relatively lower density and higher probability for having internal flaws.

For the growth of $Mg_{0.07}Zn_{0.93}O$ films, conductive Zn–Mg targets were sputtered and thus a DC power source was utilized. The DC source used in this work is an MDX 500 by Advanced Energy with a maximum power of 500 *W* and built in arc-suppression circuitry.

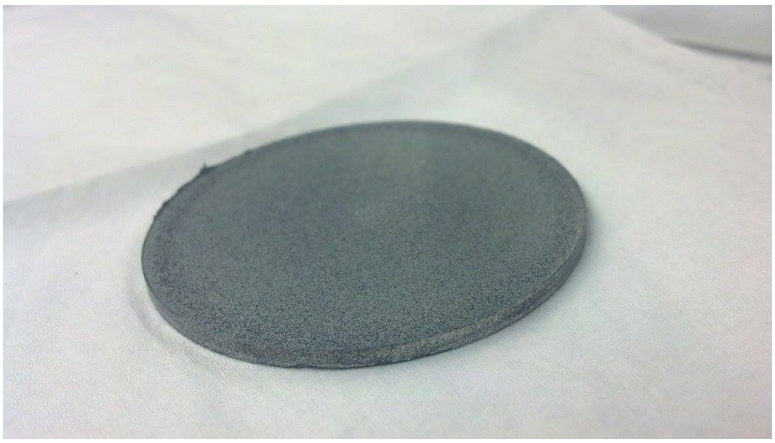

FIGURE 2.6: *A photograph of a custom made $Mg_{0.07}Zn_{0.93}O$ target, made to contain 7% Mg, pressed by a Carver hydraulic press.*

Conclusion — Many variables were shown to influence semiconductor thin-film growth and this chapter has outlined the sputtering growth method used to synthesize ZnO thin films and $Mg_{0.07}Zn_{0.93}O$ thin film alloys in addition to outlining the customized features used herein. We have shown that numerous measures were taken to ensure as much control over the growth environment as possible which in turn ensures minimal variation in experimental samples.

REFERENCES

[1] B. A. Banks, M. J. Mirtich, S. K. Rutledge, and D. M. Swec, Thin solid films **127**, 107 (1985).

[2] J. L. Edwards and R. J. Roedel, Electronics Letters **19**, 962 (1983).

[3] M. J. Ellison, *Advances in Thin Film Coatings for Optical Applications*, Vol. 6286 (Society of Photo Optical, 2006).

[4] W. R. Grove, Philosophical transactions of the Royal Society of London **142**, 87 (1852).

[5] J. T. Merz, *A History of European Thought in the Nineteenth Century* (W. Blackwood, 1912).

[6] L. Holland, *Vacuum deposition of thin films* (Wiley, 1966).

[7] P. Sigmund, Physical Review **184**, 383 (1969).

[8] A. Anders, Thin Solid Films **502**, 22 (2006).

[9] D. C. Carter, R. L. Arent, and D. J. Christie, in *50th Annual Technical Conference Proceedings* (Advanced Energy Industries, Inc., 2007).

[10] D. M. Mattox, *The Foundations of Vacuum Coating Technology* (Springer Science & Business Media, 2004).

CHAPTER 3

Optical Spectroscopy

Introduction — This chapter explores the nature of electromagnetic radiation and provides several mechanisms for the interaction of radiation and semiconducting solids. We will see that the basis for the interaction, and ultimately the transfer of energy, is a coupling between the radiation field and the fields existing within the solid structure. In spectroscopy, we experimentally observe the interaction of radiation with matter, and in this work, our semiconductors, ultimately gaining insight into the band structure of the thin films and thin-film alloys. This chapter focuses on UV-Visible absorption spectroscopy, which comprises the dual relationship between transmission and absorption of radiation in ZnO and $Mg_{0.07}Zn_{0.93}O$.

3.1 OPTICAL SPECTROSCOPY

Spectroscopy is science that deals with the interaction of radiation with matter. Historically, the interactions between electromagnetic radiation and matter were of primary interest, but spectroscopy has expanded to include acoustic waves and particle beams such as ion or electron beams. Still, electromagnetic radiation is most widely used. Electromagnetic radiation comprises a vast spectrum, including visible light, infrared, gamma rays, X-rays, ultraviolet (UV), microwave and radio-frequency radiation.

3.2 ELECTROMAGNETIC RADIATION

Electromagnetic radiation is most easily described by the wave model which involves quantities such as wavelength, frequency, velocity and amplitude. In contrast to phononic phenomenon, electromagnetic radiation propagates readily through the vacuum of space. In a vacuum, the velocity of radiation is independent of wavelength

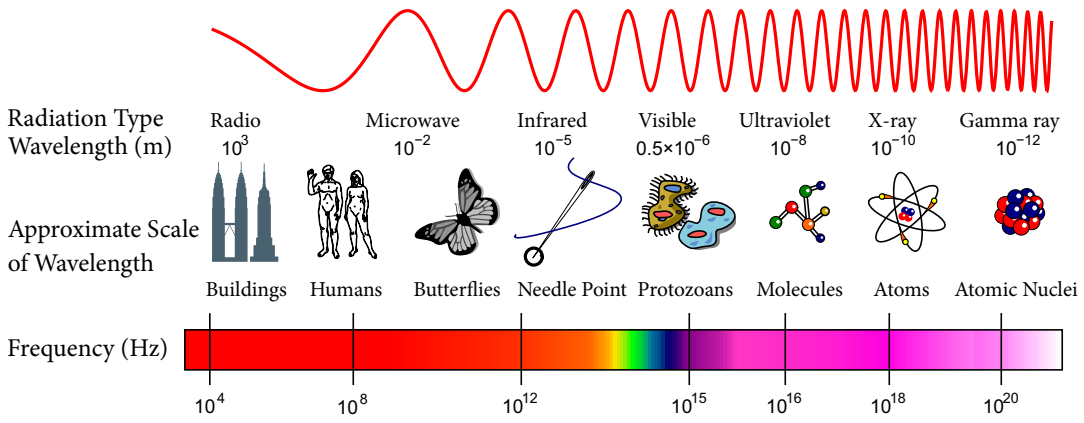

FIGURE 3.1: *The electromagnetic spectrum encompasses a vast range of energies—a range so great that a logarithmic scale is required. This spectrum has been qualitatively divided based on the methods used to generate and detect the different types of radiation. Some overlaps do occur. (Inductiveload, 2007)*

and is at its maximum—denoted by the symbol, c—and has been determined to be $2.998 \times 10^{8}\ m/s$. The velocity of radiation in air differs only slightly from c, and is written, for vacuum or air, as $c = 3 \times 10^{8} m/s$. As the density of matter increases, propagation of radiation through a medium slows by the interaction between the electromagnetic field of the radiation and the elementary particles that constitute the medium. Since frequency is fixed by the source, the wavelength must decrease as radiation passes from vacuum to denser media.

3.3 TRANSMISSION OF RADIATION

The rate at which radiation propagates through a transparent substance, as noted previously, is less than its velocity in a vacuum and depends on the kinds and concentration of atoms, ions or molecules in the medium. Therefore, the radiation must be interacting in some way with the matter. A change in frequency is not observed—so, the interaction does not involve a permanent energy transfer.

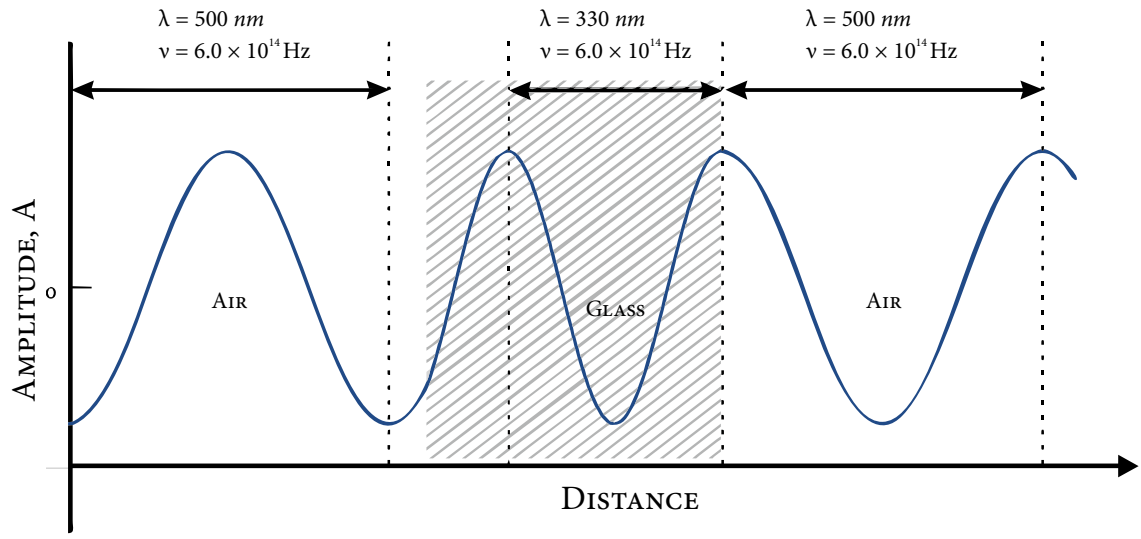

FIGURE 3.2: *As radiation passes from a less dense medium to a more dense medium a change in wavelength occurs. The reverse change occurs as the radiation re-enters the air.*

The interaction involved in transmission can be attributed to periodic polarization of the atoms, ions or molecules that constitute the medium.[1] Polarization in this context is the temporary deformation of the electron clouds associated with atoms by the alternating field of the electromagnetic radiation. The polarizability of the valence shell electrons depend on the strength of their interaction with the nucleus and intervening filled shells. Provided that the radiation is not absorbed, the energy required for polarization is only retained for 10^{-14} 10^{-15} s by the species and is re-emitted without alteration as the substance returns to its original state.[2] Since there is no net energy transfer, the frequency of the emitted radiation is unchanged, but the rate of its propagation is slowed by the time it takes for retention and re-emission to occur.

[2]Radiation from polarized particles should be emitted in all directions in a medium. If the particles are small, however, destructive interference prevents the propagation of significant amounts of radiation in any direction other than that of the original path.

The refractive index is related to polarizability and is a measure of a medium's interaction with radiation, and therefore the speed of radiation propagation, as defined by:

$$\eta(\nu) = \frac{c}{v(\nu)} \tag{3.1}$$

where $\eta(\nu)$ is the refractive index at a specific frequency, v is the velocity of the radiation in the medium and c its velocity in vacuum.

The velocity of radiation in matter is wavelength dependent and since c in Eq. 3.1 is independent of wavelength, the refractive index of a substance must also change with wavelength. The variation of refractive index with wavelength or frequency is called dispersion. Dispersion plots exhibit two types of regions, normal and anomalous. In normal dispersion, the slope is gradual, whereas in anomalous dispersion the slope is sharp.

3.4 ABSORPTION & THE SIGNIFICANCE OF RESONANCE

Anomalous dispersion always occurs at frequencies that correspond to the natural harmonic frequency associated with ionic, inter-atomic or orbital perturbation of a substance. At such a frequency, resonance occurs and a permanent energy transfer takes place.

Resonance is a requirement for the absorption of radiation and depends on both the frequency of the driving electromagnetic field and the natural frequency of the oscillator. The absorption of UV-visible radiation by electrons can be described classically by the frequency-dependent dielectric function of a material.[2] Furthermore, light can only couple to optical phonons very close to the center of the Brillouin zone at $k = 0$ and the electromagnetic excitation of such a mode corresponds to the introduction of a time-varying dipole within the crystal.

3.5 GENERAL SPECTROSCOPIC TECHNIQUES

In absorption spectroscopy, we measure the amount of radiation absorbed as a function of wavelength. In semiconducting solids, the onset of the absorption of radiation indicates that the electromagnetic energy meets that required by electrons in overcoming the bandgap energy. In photoluminescence spectroscopy, the emission of photons is measured after absorption which yield information about radiative relaxation pathways in a sample. Furthermore, Raman spectroscopy uses inelastic scattering to glean information about the vibrational modes of a sample. Absorption, photoluminescence and Raman spectroscopy generally yield complementary information about a sample and are usually used in conjunction, however, the primary focus of this work is absorption spectroscopy.

3.6 TRANSMITTANCE & ABSORBANCE

In practice, calculating the energy of radiation absorbed is determined by the experimental measurement of transmittance, T, of samples. The transmittance of a material is given by the following equation which is a ratio of the intensities of incoming, I_o, and outgoing, I', electromagnetic radiation.

$$T = \frac{I'}{I_o} \tag{3.2}$$

Reflection, R, also occurs at air/sample/substrate interfaces during a measurement, along with multiple internal reflections within the film itself. Taking these into consideration, the transmittance is then given by the following:[3]

$$T = \frac{I'}{I_o} = \frac{(1-R)^2 e^{\frac{-4\pi\nu\kappa\chi}{c}}}{(1-R^2)e^{\frac{-8\pi\nu\kappa\chi}{c}}} = \frac{(1-R)^2 e^{\frac{-\alpha t}{c}}}{(1-R^2)e^{\frac{-2\alpha t}{c}}} \tag{3.3}$$

where $\alpha = \frac{4\pi\nu\kappa}{c}$ is equivalent to the absorption coefficient of the film described above.

For semiconductor materials, the reflectivity, R is negligible even near the absorption edge.[4] For the purposes of band edge analysis, the transmittance, T, of a semiconductor with film thickness, t, can be expressed as an approximation of the form:

$$T = e^{-\alpha t} \tag{3.4}$$

Consequently, with measured transmittance and film thickness, t, the absorption coefficient, α, can be obtained:

$$\alpha = -t^{-1} ln T \tag{3.5}$$

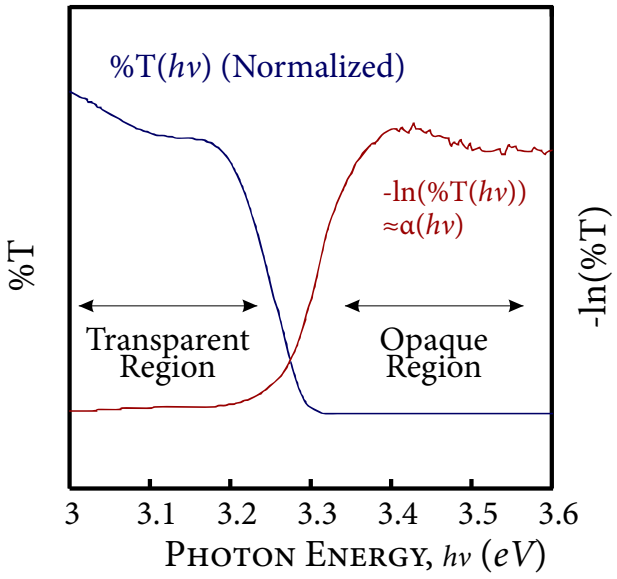

FIGURE 3.3: *Normalized transmission of electromagnetic radiation in ZnO thin film as a function of photon energy (blue) and corresponding absorption as a function of photon energy (red). The conversion to absorption is a simple negative logarithm. Note the film thickness has not been included in the conversion.*

We will see in the next chapter how the experimentally determined absorption coefficient relates to theoretical models that allow us to analyze the band structure of ZnO and $Mg_{0.07}Zn_{0.93}O$.

Conclusion — In this chapter we have seen that the interaction of radiation with semiconductors in controlled experiments can yield valuable information about the electronic structure therein. In absorption spectroscopy we measure the intensity of radiation transmitted to calculate the amount of radiation absorbed, or absorption coefficient. The absorption coefficient can be used to gain valuable information about the band structure of semiconductors and alloys. Techniques for analyzing data from absorption spectroscopy are given in the following chapter.

REFERENCES

[1] D. A. Skoog, F. J. Holler, and S. R. Crouch, *Principles of Instrumental Analysis*, 6th ed. (Brooks Cole, Belmont, CA, 2006).

[2] P. Hofmann, *Solid State Physics: An Introduction* (John Wiley & Sons, 2011).

[3] J. I. Pankove, *Optical processes in semiconductors* (Prentice-Hall, Englewood Cliffs, NJ, 1971).

[4] S. T. Tan, B. J. Chen, X. W. Sun, X. Hu, X. H. Zhang, and S. J. Chua, Journal of Crystal Growth **281**, 571 (2005).

CHAPTER 4

Analytical Techniques: Key Features in Demonstrative Spectra

Introduction — We have seen that the transition from transmission of radiation to absorption in a semiconductor corresponds to the bandgap. The slope of this transition is indicative of band-edge quality. From the spectra acquired we can also extract information about the band structure of the semiconductor. This is because features in the spectra are directly related to allowed transitions between electronic states. The following sections contain a brief overview of some of the transitions observed in absorption spectroscopy including band-to-band, excitonic, and impurity-band transitions. These transitions will be described in conjunction with their corresponding features in the absorption spectra acquired in this work. It is the goal of this work to resolve many of the components that constitute the band-edge in the spectra of ZnO and $Mg_{0.07}Zn_{0.93}O$.

4.1 BAND-EDGE ANALYSIS

The bandgap is defined by the energetic region at which a semiconductor begins to absorb radiation. In spectroscopy, this region corresponds to the drastic increase in the absorption coefficient and is generally related to transitions involving the valence band maximum and conduction band minimum. Qualitatively, the band-edge defines the slope of this transition. A sharp band-edge corresponds to a well defined bandgap or sharp slope of the transition to absorption. A soft band-edge defines the opposite.

Electron transitions are subject to certain selection rules, and the most probable transition will give the most intense signal in absorption spectroscopy. The most likely transition may not always be fundamental bandgap transitions, and is generally not the case. Thus, the estimation of the fundamental energy gap from the absorption

edge or "band-edge" is not always an easy task. Though fundamental transitions occur, transitions into preferential states, such as defect states or excitonic states, conceal information about other transitions, especially in a thermally excited environment, rendering the determination of the fundamental energy gap a problematical task.

For this reason, a distinction between the fundamental gap and the optical gap is made. The fundamental gap refers to band to band transitions, whereas the optical gap refers to the energetic transition into available energy states lower than the fundamental gap energy, such as defect states or excitonic states.

It is the goal of this work to resolve many of the components that constitute the band-edge in ZnO and $Mg_{0.07}Zn_{0.93}O$. The following figures show the band-edge as a convolution of several possible transitions including band-tail transitions, corresponding to the optical gap, excitonic transitions, corresponding to a resonance peak, and fundamental gap transitions, which is generally lost in the convolution. The following sections will outline the theory and the mathematical formulations for modeling these transitions individually.

4.2 FUNDAMENTAL ABSORPTION

Fundamental absorption describes energetic transitions from band to band. In the absence of thermal excitation and defect states, resonance occurs at a distinct photon frequency. Thus, fundamental absorption manifests itself as a sharp rise in absorbance and is often used to determine the fundamental gap of a semiconductor.

The absorption coefficient, α, for a given photon energy, $h\nu$, is a statistical quantity proportional to the probability for the transition from the initial state to the final state, P_{if}, to the density of electrons in the initial state, n_i, and to the density of states of

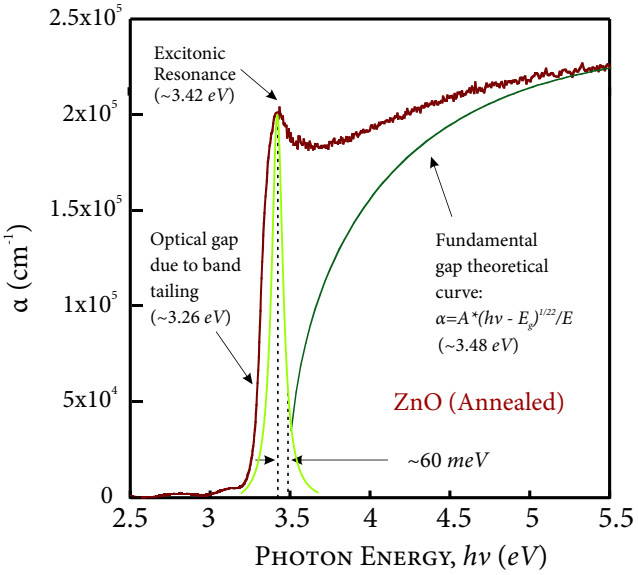

FIGURE 4.1: *Absorption spectrum of ZnO thin film studied in this work taken at 294 K. As the photon energy increases, the bandgap of the film is characterized by the significant increase in absorption. This occurs at the optical gap due to the presence of defects and excitonic states. The fundamental gap, following the form of equation 4.7 is lost in the spectra. Exciton transitions occur when the photon energy is less than the bandgap energy.*

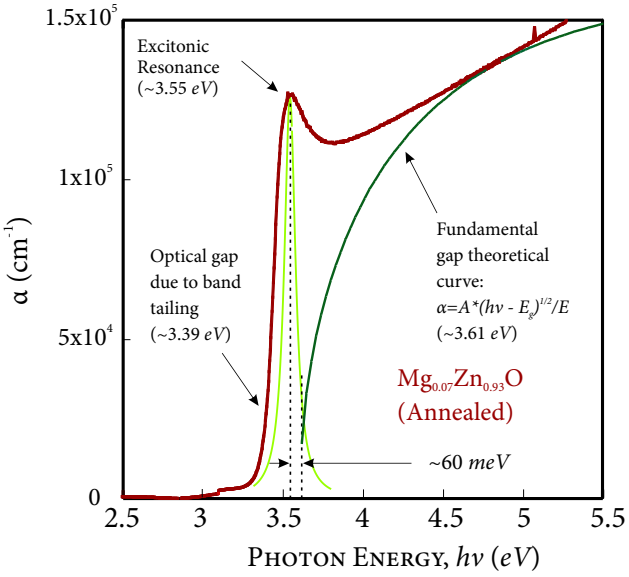

FIGURE 4.2: *Absorption spectrum of $Mg_{0.07}Zn_{0.93}O$ thin film studied in this work taken at 294 K. As the photon energy increases, the bandgap of the film is characterized by the significant increase in absorption. This occurs at the optical gap due to the presence of defects and excitonic states. The fundamental gap, following the form of equation 4.7 is lost in the spectra. Exciton transitions occur when the photon energy is less than the bandgap energy.*

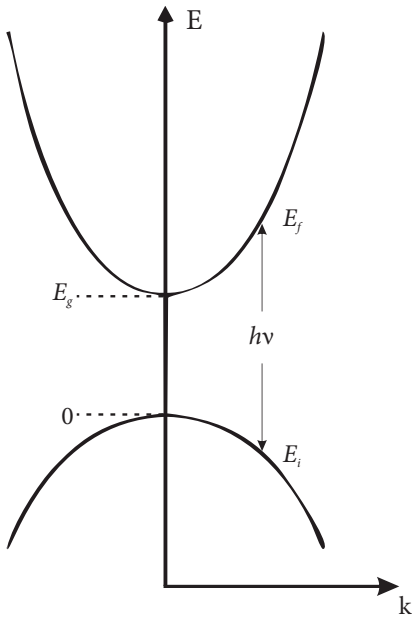

FIGURE 4.3: *Direct transition at the fundamental gap.*

available final states, n_f, summed for all possible transitions between states separated by an energy difference equal to $h\nu$.[1]

$$\alpha(h\nu) = A \sum P_{if} n_i n_f \tag{4.1}$$

Next, we assume that all the lower states are filled and that all the upper states are empty—only strictly true at 0 K—and consider transitions between two direct valleys at $k = 0$. Every initial state is associated with a final state as illustrated in Fig. 4.3, as follows:

$$E_f = h\nu - |E_i| \tag{4.2}$$

In parabolic bands, however

$$E_f - E_g = \frac{\hbar^2 k^2}{2m_e^*} \tag{4.3}$$

and

$$E_i = \frac{\hbar^2 k^2}{2m_h^*} \tag{4.4}$$

Therefore,

$$h\nu - E_g = \frac{\hbar^2 k^2}{2}\left(\frac{1}{m_e^*} + \frac{1}{m_h^*}\right) \tag{4.5}$$

Furthermore, Pankove calculates the density of states associated with the transition as:

$$N(h\nu)d(h\nu) = \frac{8^2 dk}{(2\pi)^3} = \frac{(2m_r)^{3/2}}{2\pi^2\hbar^3}(h\nu - E_g)^{1/2}d(h\nu) \tag{4.6}$$

where m_r is the reduced mass of the electron and hole given as $1/m_r = 1/m_e^* + 1/m_h^*$. Finally, the absorption coefficient, given here for a direct bandgap semiconductor, is given by:[2]

$$\alpha(h\nu) = A^*(h\nu - E_g)^{1/2} \tag{4.7}$$

where

$$A^* = \frac{q^2\left(2\frac{m_h^* m_e^*}{m_h^* + m_e^*}\right)^{3/2}}{\eta c h^2 m_e^*} \tag{4.8}$$

η being the index of refraction.

The functional form corresponding to transitions of this nature can be seen in Fig. 4.1 given by the dark green curve, marked as the fundamental gap.

4.3 EXCITONIC TRANSITIONS

Transitions to excitonic states in a semiconductor occur with high probability as seen in Fig. 4.1, thus making the analysis of excitonic resonances in absorption spectra key in understanding the dynamics at the band-edge. In ZnO and $Mg_{0.07}Zn_{0.93}O$, these

transitions occur for energies below the fundamental gap as shown in Eq. 4.9 and manifest in absorption spectra as a sharp resonance peak.

$$h\nu = E_g - E_x \tag{4.9}$$

where E_x is the binding energy of the exciton. See Fig. 4.4.

Fig. 4.4 shows the location of an exciton energy level in relation to the conduction band. As seen in Fig. 4.5, the width of this peak broadens with temperature until it becomes the dominant feature of the absorption edge. This phenomenon is described in the following subsection.

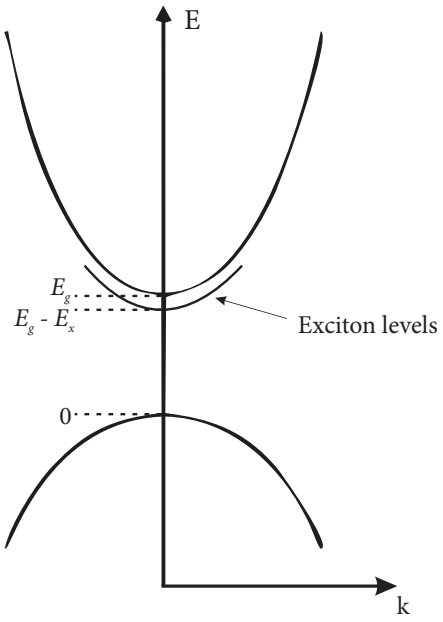

FIGURE 4.4: *Exciton levels with respect to the conduction band edge for a direct-gap system at $k = 0$. Excitons can have translational kinetic energy.*

The functional form corresponding to excitonic transitions can be seen in Fig. 4.1 4.2 given by the light green peak marked as excitonic resonance.

4.3.1 *Peak Broadening in Spectroscopy*

At zero temperature, the transition of an electron between two discrete single-valued energy states—for example, transition between the valence band and an excitonic energy level in a semiconductor–will, in principle, correspond to a peak of line width approaching zero, especially if a material is sufficiently pure.[1] Excitonic transitions in absorption spectra however commonly appear as a broadened peak instead of a thin spike. This phenomenon is known as peak broadening.

In general, there are several sources of broadening in absorption or emission spectra including, the uncertainty effect, the Doppler effect, and thermal effects.

In absorption spectra of semiconductors, thermal broadening effects or phonon broadening is caused by electron-phonon interactions, which will be discussed in detail in the following chapter. In semiconductors, phonon broadening can be observed in exciton peaks even at room temperature and especially so at higher temperatures as shown in absorption spectra in Fig. 4.5.

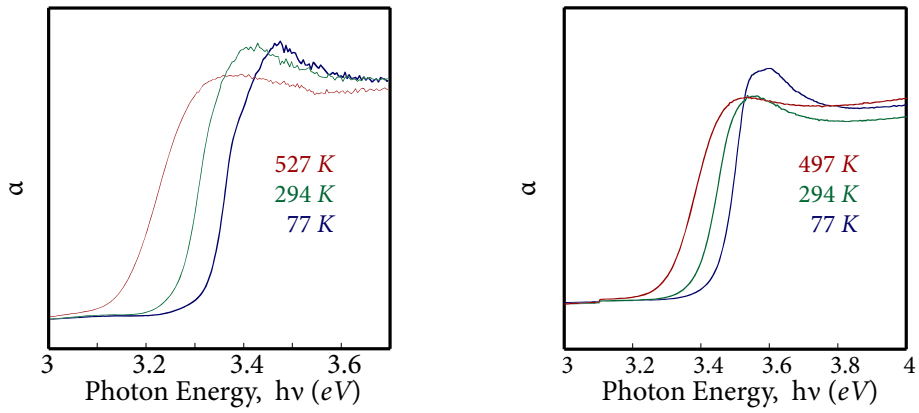

FIGURE 4.5: *Exciton peaks in absorption spectra of ZnO and $Mg_{0.07}Zn_{0.93}O$ at 77 (blue), 294 (green) and 527 and 497 K (red), respectively. At higher temperatures, the exciton peak broadens significantly and becomes the domininant feature in the spectra.*

The band-edge region is a convolution of several distinct transitions as mentioned previously, and at higher temperatures, the components of the band-edge corresponding to the broadened exciton peak and the tailing states due to defects are unresolved. This effect is described in more detail the following section.

4.4 BAND-TAIL TRANSITIONS & URBACH ANALYSIS

The final component to the band-edge includes band-tail transitions. The presence of defects, previously discussed in Sec. 1.6.1, also results in states at energies less than the fundamental gap. The density of these defect states increases exponentially toward the fundamental gap. Consequently, as photon energy approaches the gap energy, the number of absorption events also increases exponentially.

This results in further broadening of the absorption edge and is especially observed in alloys. For this reason, this effect is commonly referred to as alloy broadening. The exponential increase in absorption at the band-edge was first reported by Urbach in 1953 and has been observed in heavily doped semiconductors, amorphous semiconductors and semiconductor alloys.

In practice, the correlation between the exponentially increasing absorption edge and the exponential density of energy states at the band-edge can be obtained.

Consider electron transitions from energy E_v in the parabolic valence band to energy E' in the exponential tail of conduction band, as shown in Fig. 1.8. The initial and final density of states is then given by $N_i \propto E_i^{1/2}$ and $N_f \propto e^{E'/E_u}$, respectively, *where E_u is an empirical parameter describing the density of in-gap states.* The absorption coefficient corresponding to this type of electronic transition is proportional to the product of the densities of initial and final states integrated over all possible transitions for a given energy, E:[1]

$$\alpha(h\nu) = A \int_{\xi}^{h\nu-\xi} |E_v|^{1/2} e^{E/E_u} dE \tag{4.10}$$

where A is a constant and ξ is an infinitesimal amount of energy. Apply the constraint of energy conservation, $E_v = E' - E$, and making the following change of variable:

$$x = \frac{h\nu - E}{E_u} \tag{4.11}$$

Eq. 4.10 can be written as

$$\alpha(h\nu) = Ae^{h\nu/E_u}(E_u)^{3/2}\int_{(h\nu+\xi)/E_u}^{\xi/E_u} x^{1/2}e^{-x}dx \tag{4.12}$$

The integral part is independent of E since $E \ll E_u$ and therefore,

$$\alpha(h\nu) = C^* e^{E/E_u} \tag{4.13}$$

Or,

$$ln(\alpha(h\nu)) = C^{**} + {}^{E}/_{E_u} \tag{4.14}$$

Where $C*$ and C^{**} are constants.

Hence, the slope of the absorption edge on a semilogarithmic plot yields a straight line. The reciprocal of the slope obtained then gives the value of E_u, as illustrated in Fig. 4.6.

Combining Eq. 4.14 with Eq. 3.5 illustrates the analytic pathway between transmittance and the parameter, E_u, as follows:

$$ln(-lnTt^{-1}) = C'' + {}^{E}/_{E_u} \tag{4.15}$$

and,

$$ln(-lnT) - ln(t) = C'' + {}^{E}/_{E_u} \tag{4.16}$$

finally, the film thickness is absorbed as a constant and the inverse slope of the double semilogarthmic plot of normalized transmission, as a function of photon energy, yields the parameter, E_u, as follows:

$$ln(-lnT) = C''' + \left(\frac{1}{E_u}\right)E \tag{4.17}$$

The Urbach Energy — The parameter E_u is commonly referred to as the Urbach energy and is a measure of the density of localized sub-gap states.

The Urbach energy parameter does not distinguish the *source* of these states, however, and generally report a value that includes structural defects as well as interstitial and vacancy defects.[3] At higher temperatures, exciton peak broadening extends the band-edge and contributes to the Urbach energy parameter as well.

In this work, exponential absorption tails have been observed in both ZnO and $Mg_{0.07}Zn_{0.93}O$ films and Urbach energies, E_u, have been extrapolated in order to further investigate the nature of these localized sub-gap states.

Furthermore, the nature of structural defect states in ZnO and $Mg_{0.07}Zn_{0.93}O$ is the primary focus of this work and the removal of intersitial and vacancy defect contribution to the Urbach energy was necessary. This is discussed in sections following.

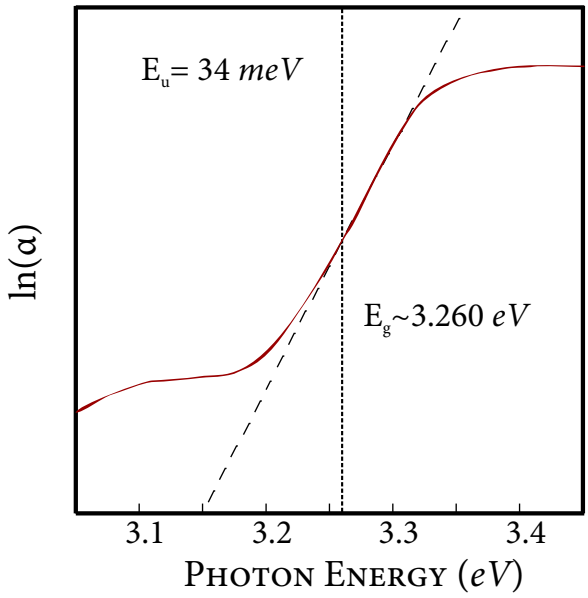

FIGURE 4.6: *The inverse slope of the absoprtion edge of a semilogarithmic plot of absorption of ZnO (taken at 294 K) yields the Urbach energy parameter. The optical gap is shown for reference. $Mg_{0.07}Zn_{0.93}O$ analysis follows similarly.*

4.5 DETERMINING THE OPTICAL GAP

There are two well-known methods used for determining the optical gap. Namely, the linear fitting analysis and the derivative or inflection point method. The linear fitting analysis yields a straight line over the energy range above E_g at the band-edge and will intersect the energy axis at the value of E_g. Therefore, the value of bandgap energy, E_g, can be extrapolated via a fitting to the linear region of the plot. This approach is well known and has been widely used for various semiconductor materials. However, this analysis is limited by its ambiguity when applied to materials which experience band tailing, such as the alloys presented in this work. As mentioned, tailing broadens the absorption edge and eliminates the somewhat abrupt cutoff otherwise expected at the absorption edge. When an absorption edge is not sharply defined, the usual extrapolation of the bandgap energy via linear fitting may not render accurate results. Due to the lack of a well defined linear region, linear fittings can be performed across an arbitrary range of the band-edge, leading to varying extrapolated values

of the bandgap. Given the limitations addressed, the present work uses the second procedure for determining the bandgap of the samples presented here.

4.5.1 *The Derivative Method*

Start with the Ridley's model of the absorption coefficient, α:[4]

$$\alpha = C^* \frac{1}{E\eta_r}(E - E_g)^{1/2} \tag{4.18}$$

where $C^* = {}^8/_3 \beta a_H^2 R_H^2 \frac{p_{cv}^2}{2m} \left(\frac{2m_r^*}{\hbar^2}\right)^{3/2}$

According to Eq. 3.4, the transmittance, T, can be expressed as:

$$T = \exp\left\{C^* \frac{1}{E\eta_r}(E - E_g)^{1/2} t^{-1}\right\} = \exp\left\{C^{**} \frac{1}{E\eta_r}(E - E_g)^{1/2}\right\} \tag{4.19}$$

Next, the first order derivative of the transmittance T with respect to incident photon energy, E, is performed:[5]

$$\begin{aligned} \frac{dT}{dE} = &-C^{**} exp\left[-C^{**} \frac{1}{E\eta_r}\sqrt{E - E_g}\right] \\ &\times \left[\frac{-1}{E^2\eta_r}\sqrt{E - E_g} - \frac{d\eta_r}{dE}\frac{\sqrt{E - E_g}}{E\eta_r^2} + \frac{1}{2\eta_r}\frac{1}{E\sqrt{E - E_g}}\right] \end{aligned} \tag{4.20}$$

Assuming that η_r does not blow up (which is a reasonable assumption) at the point where the energy of incident light E approaches that of the bandgap, i.e. $E \longrightarrow E_g$, Eq. 4.20 yields:

$$\lim_{E \longrightarrow E_g} \frac{dT}{dE} = -C^{**}\left(-0 - 0 + {}^1/_0\right) \longrightarrow -\infty \tag{4.21}$$

Which will appear in the plot of $\frac{dT}{dE}$ versus E as a sharp inflection point where the incident photon energy equals the bandgap energy, E_g, of the material.

This method has the advantage of being applicable to materials with or without a well defined absorption edge, as shown in Fig 4.7. On the other hand, the energy dependent refractive index η_r nor film thickness, t plays any role in determining where the inflection point occurs. Thus, no approximation of a constant η_r is needed.

The derivative analysis has shown success in previous studies of determining semiconductor bandgaps.[6–8]

It is worth noting that both the conventional and the derivative method analysis discussed above are based on Eq. 3.5, which neglected the reflection occurring at both the air/film interface and the film/substrate interfaces, along with the multiple internal reflections occurring within the film. However, when the reflection at all the interfaces are taken into consideration, $\alpha^2 E^2$ is no longer directly proportional to $E - E_g$, rendering the theoretical foundation of the conventional linear fitting analysis no longer valid. The derivative method, however, retains its validity.

4.6 ANALYSIS OF DEFECT REMOVAL

As mentioned previously the Urbach parameter does not distinguish between structural defects, interstitial defects, vacancies, and others and in many cases, structural defects and impurities are interrelated.

Structural defects are bulk defects produced through the propagation of the microscopic flaws in the lattice of a solid. For crystals with planar defects, such as polycrystalline solids, the grain boundary marks the interface between two misaligned portions of the crystal. The size of the individual microcrystals (or grains) that comprise a larger aggregate greatly affects many of its properties.

Energy is required to form a defect surface, thus, grains tend to grow in size in favor of smaller grains to minimize energy. This growth process occurs by diffusion, which is accelerated at high temperatures.[9] The density of atoms at a solid surface, or

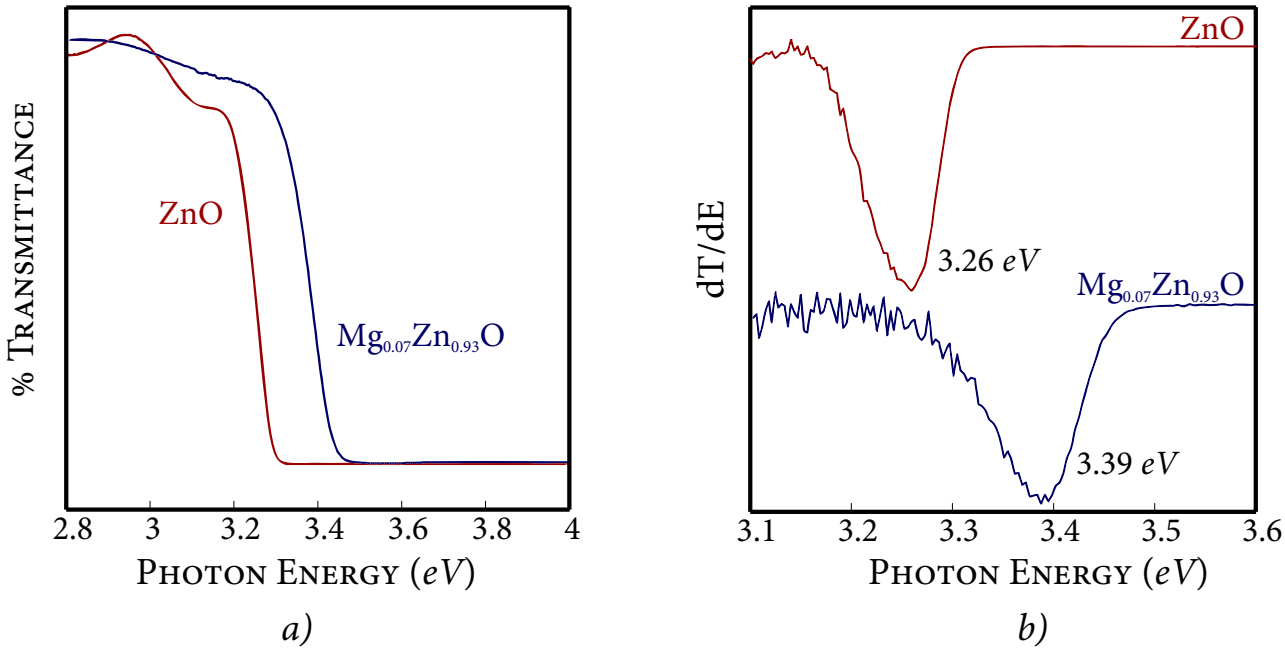

Figure 4.7: *(a) Transmittance spectra and (b) derivative method of optical gap determindation for ZnO and $Mg_{0.07}Zn_{0.93}O$ thin film at 294 K. The inflection point of $Mg_{0.07}Zn_{0.93}O$ is slightly less defined than that of ZnO due to alloy broadening of the absorption edge.*

in the region surrounding a grain boundary is always smaller than density within it. This is due to atoms at these regions containing dangling bonds, which are described as being "coordinatively unsaturated." In addition to bulk, planar, and linear classes of crystalline imperfections that involve perturbations of large groups of lattice atoms, point defects are also present.

As the temperature of the crystal is increased, the atoms in the crystal vibrate about their equilibrium positions which prompt the atomic diffusion of these points defects, which include interstitial impurities and vacancies. Many studies have shown that annealing ZnO and $Mg_{0.07}Zn_{0.93}O$ semiconductor thin films improves crystal quality by removing a majority of interstitial and vacancy defects associated with zinc and oxygen.

Preliminary research conducted via SEM and PL studies by Thapa et al. showed results indicating that the annealing process diminishes the defects in films relative to the as-grown samples. The annealing program shown in Fig. 4.8, taken from ongoing work mentioned, was implemented on both ZnO and $Mg_{0.07}Zn_{0.93}O$ samples and the program was run in an Argon-only environment using a Lindberg/Blue quartz tube furnace.

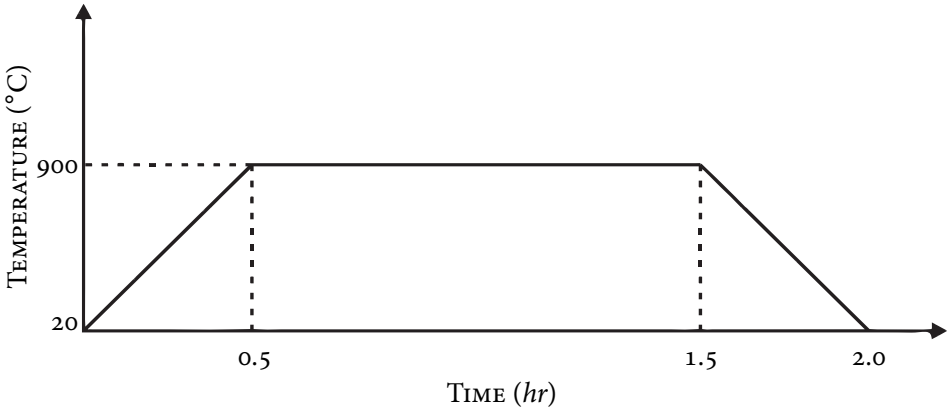

FIGURE 4.8: *The temperature program used for annealing samples studied in this work. Samples placed in 900°C under Argon for one hour have been shown to have most intersitial and vacancy defects removed.*

SEM results from Thapa et al. shown in Fig. 4.9 highlight morphological changes incurred in as-grown ZnO thin films through annealing. In Fig. 4.9a, the image of the as-grown film, under high magnification, reveals that the film consists of granular morphology with significant secondary nucleation, i.e. secondary crystallization from pre-existing crystals. Furthermore, the grains are not well defined, which indicate an increased presence of defects. In contrast, Fig. 4.9b shows annealed films which display well-defined grains and much improved morphology.

While there is much advantage in analyzing an image, SEM does not directly facilitate insight into the specific nature of defects in thin films.

Consequently, PL studies were conducted on as-grown and annealed films in order to uncover the nature of these defects. Fig. 4.10 shows PL conducted on as-grown

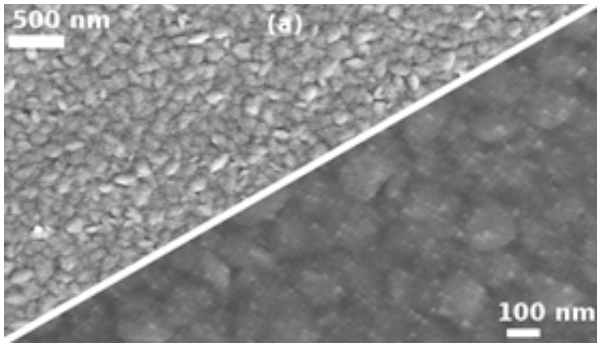

a)

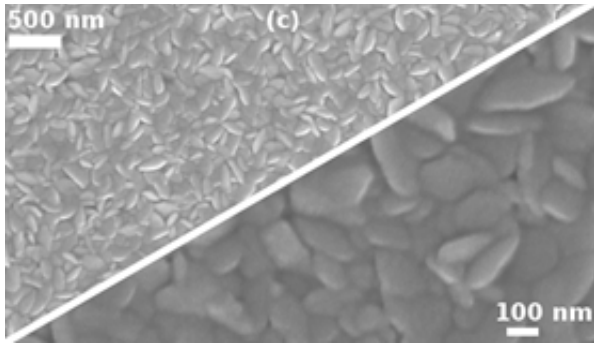

b)

FIGURE 4.9: *SEM image of ZnO films: (a) as-grown and (b) Ar annealed, both under low and high magnifications to highlight surface morphology.*

ZnO film in comparison to PL conducted on annealed ZnO film. It is clear from the figures that the annealed ZnO film shows significantly enhanced PL after undergoing annealing treatment.

As seen in Fig. 4.10a, the PL spectra of as-grown ZnO shows a very broad emission, which has been deconvolved using voigt profile fitting, indicating the existence of two peaks—one in the visible region at 2.80 eV and the other one in the UV range at 3.25 eV. PL emission of this nature, showing two emission peaks, has been found to be characteristic of most studies of ZnO.[10–12]

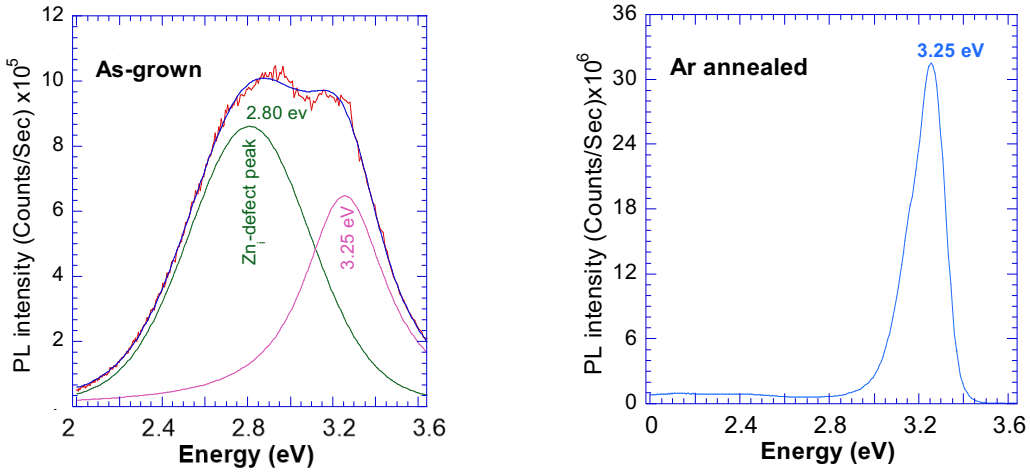

a) *b)*

FIGURE 4.10: *PL spectra of the ZnO films: (a) as grown film showing two peaks at 2.80 and 3.25 eV, were obtained with a voigt profile fitting to the experimental curve. The 3.25 eV is attributed to UV band-edge emission and 2.80 eV is due to Zn_i related defects. (b) Ar annealed ZnO film showing the significantly enhanced UV PL with nearly quenched visible emission peak.*

In many studies, the 3.25 eV emission band is typically attributed to excitonic recombination while the origin of the 2.80 eV emission is usually attributed to Zn-interstitial- (Zn_i-) related defects.[10,13–15]

Fig. 4.10b shows the Ar-annealed ZnO film displaying significantly enhanced UV PL, with a nearly completely quenched visible emission peak, which indicates the removal of Zn_i-related defects. This improvement in PL emission corresponds to the improved morphology shown in Fig. 4.9b.

The comparison of annealed films to as-grown films studied here corroborates this improvement in film quality through the straightforward analysis of absorption spectra.[16,17] Shown in Fig. 4.11, improved film quality corresponds to reduced alloy broadening of the band-edge, a well-defined bandgap energy via derivative analysis, and a decrease in the Urbach energy parameter, indicating a reduction of point defect-related in-gap states.

Similar to ZnO, $Mg_{0.07}Zn_{0.93}O$ is expected to exhibit the same trend but, in addition, we may expect the introduction of Mg_i-related defect complexes. Finally, the results of the analysis of as-grown and annealed ZnO $Mg_{0.07}Zn_{0.93}O$ samples are displayed in Tab. 4.1.

The presence of Zn_i in the thin flim studied here can be attributed to the DC sputtering technique used. This growth technique is commonly reported in literature to lead to the growth of Zn-rich films, thereby favoring the formation of Zn_i-related defects.[18–20] This can be understood by noting that sputtering involves the competing processes of target oxidation and removal of target material. To achieve sputtering growth, target material must be removed at a sufficient rate to prevent oxide overcoat formation. However, by removing target material at a higher rate than the oxidation process occurs, the sputtered material may not completely oxidize. The net result of these competing processes is a Zn-rich film.

However, the focus of this work is not defects themselves, but to illustrate the analytical process involved in studying them. In this work, annealing was performed prior to further Urbach analysis in order to facilitate specificity in experimental discussion.

TABLE 4.1: *Comparison of as-grown versus annealed optical gap and Urbach energy values at room temperature for ZnO and $Mg_{0.07}Zn_{0.93}O$.*

		E_g (eV)	E_u (meV)
ZnO	As-Grown	3.20	84
	Annealed	3.26	34
MgZnO	As-Grown	3.37	108
	Annealed	3.39	50

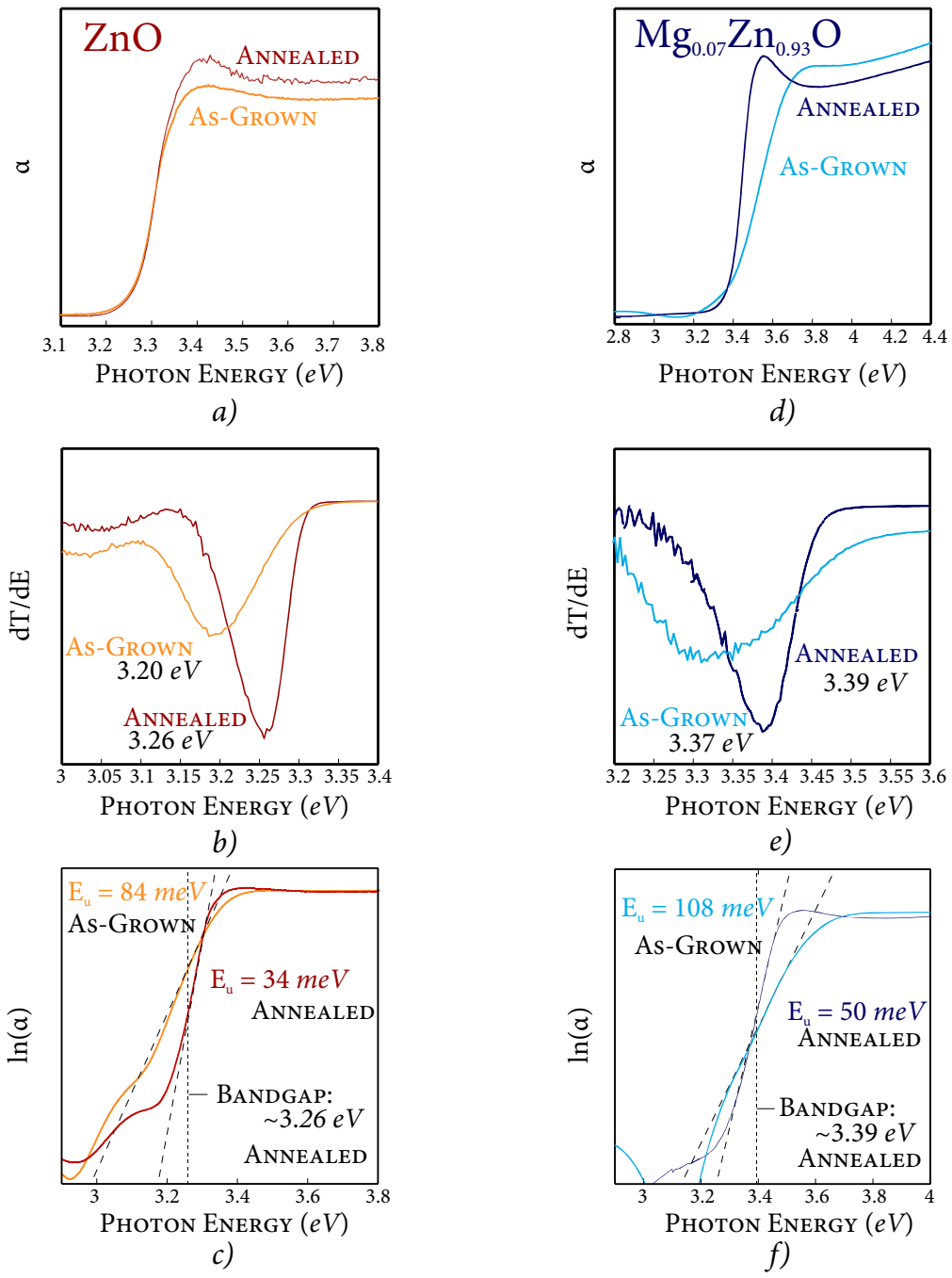

FIGURE 4.11: *Various analytical techniques applied to ZnO (a)–(c) and $Mg_{0.07}Zn_{0.93}O$ (d)–(f) after annealing under Argon. In the absorbance spectra of (a) and (d), the band edge is seen to improve, specifically an improvement in excitonic resonance in ZnO and a sharper absorption edge in $Mg_{0.07}Zn_{0.93}O$. In (b) and (e), the inflection point defining the bandgap energy in the derivative method is more clearly defined. In (c) and (f), the Urbach energy parameter, quantifying the density of in-gap states, shows a marked reduction of approximately 50-percent in both ZnO and $Mg_{0.07}Zn_{0.93}O$.*

4.7 DISCUSSION OF RESULTS FROM TEMPERATURE DEPENDENT ABSORPTION SPECTRA & ANALYSIS:

The analytical methods presented in the previous sections are useful in investigating the band-edge of ZnO and $Mg_{0.07}Zn_{0.93}O$. However, in order to deconvolve the contribution of defects and phonon broadening to the Urbach energy parameter, the Urbach energy behavior as a function of temperature was investigated.

In the lower limit of temperature, at 77 *K*, most vibrations are removed from the lattice. Thus, the phonon modes are said to be "frozen" as illustrated in Fig. 4.12. Due to the small variance in the phonon population, resonance leading to absorption occurs at relatively well-defined energies.

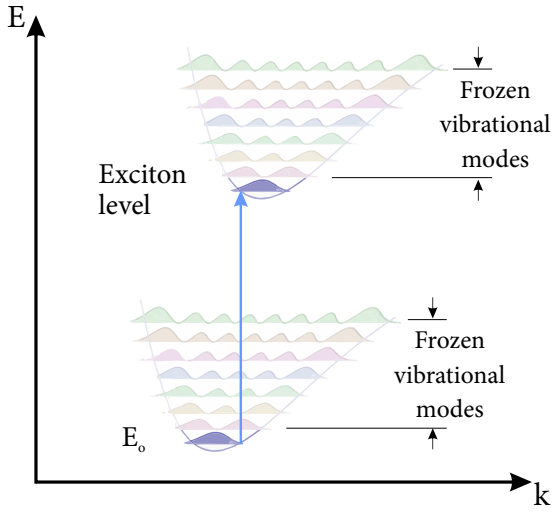

FIGURE 4.12: *"Frozen" vibrational modes at lower limits of temperature.*

In principle, the absorption peak is significantly sharpened but may still show broadening due to crystal imperfections.[21] This is illustrated by the spectra taken at 77 *K* in Fig. 4.13.

As temperature is increased, vibrational modes are no longer frozen. Thermal excitation increases the phonon population and results in the possibility of resonance with a wider range of energies. This is manifest in absorption spectra as a broadened

band-edge and in the broadening of resonance peaks, such as exciton peaks.[22] This phenomena is similar to alloy broadening seen at the band-edge given that their underlying cause is potential fluctuation—static[3] in the case of alloy broadening and dynamic in the case of thermal broadening.

The following sections are dedicated to the temperature dependent spectra and analysis. The spectra for $Mg_{0.07}Zn_{0.93}O$ was similar to that of ZnO and only representative spectra of ZnO are shown. Fig. 4.13 shows the absorption spectra as temperature varies from 77–527 *K*. As can be seen in the figure, the exciton peak broadens with increasing temperature and becomes increasingly convolved with the structural defect tail.

Fig. 4.14 shows the results of derivative analysis and Fig. 4.15 shows the Urbach energy analysis. Results are compiled in Tab. 4.2. As seen in Fig. 4.14 as temperature is increased, the well width of the gap inflection point increases as the well depth decreases.

In essence, at higher temperatures the optical gap becomes less defined. In Fig. 4.15 the slopes of the semilogarithmic plots are is seen to increase with decreasing temperature. Since the slope is inversely proportional to the Urbach energy and in-gap states, we see a diminished presence of in-gap states with decreasing temperature as expected. The results of the analysis of temperature dependent data, specifically the values of the optical gap and Urbach energy, are shown in Tab. 4.2.

[3]Defect-related energy levels are assumed to be temperature-independent in this work, and thus, static in nature.

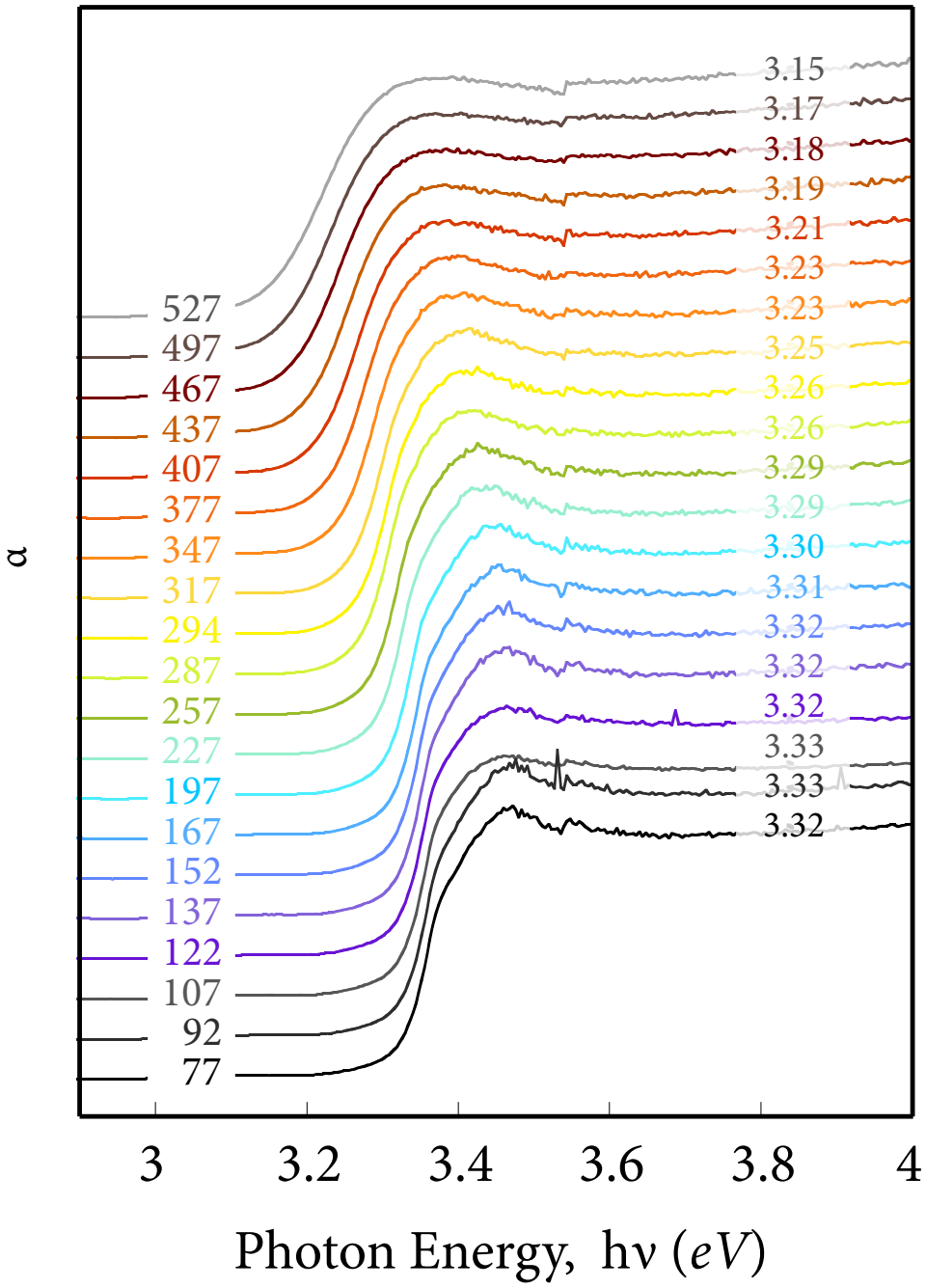

FIGURE 4.13: *Absorption spectra of ZnO as temperature varies from 77–527 K. The exciton peak broadens with increasing temperature and becomes increasingly convolved with structural defect states. Values for the resonance peak are given in Tab. 4.2.*

4.7.1 *Derivative Analysis as a Function of Temperature*

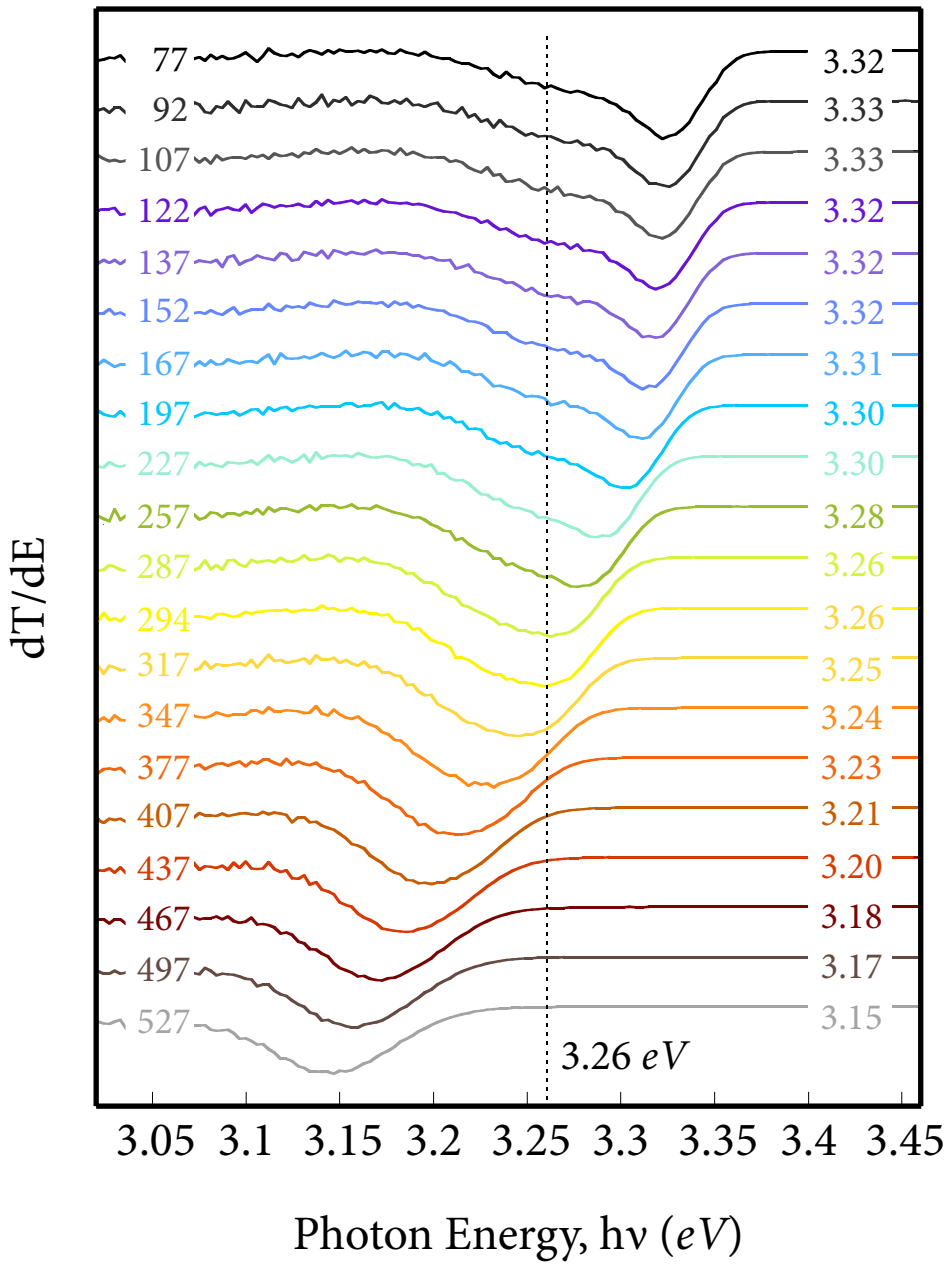

FIGURE 4.14: *Derivative analysis of ZnO as a function of temperature. At 77 K the value of the optical gap is 3.32 eV and decreases to a minimum of 3.15 eV at 527 K. The dotted line indicates the optical gap energy, 3.26 eV, at room temperature, 294 K.*

4.7.2 *Urbach Analysis as a Function of Temperature*

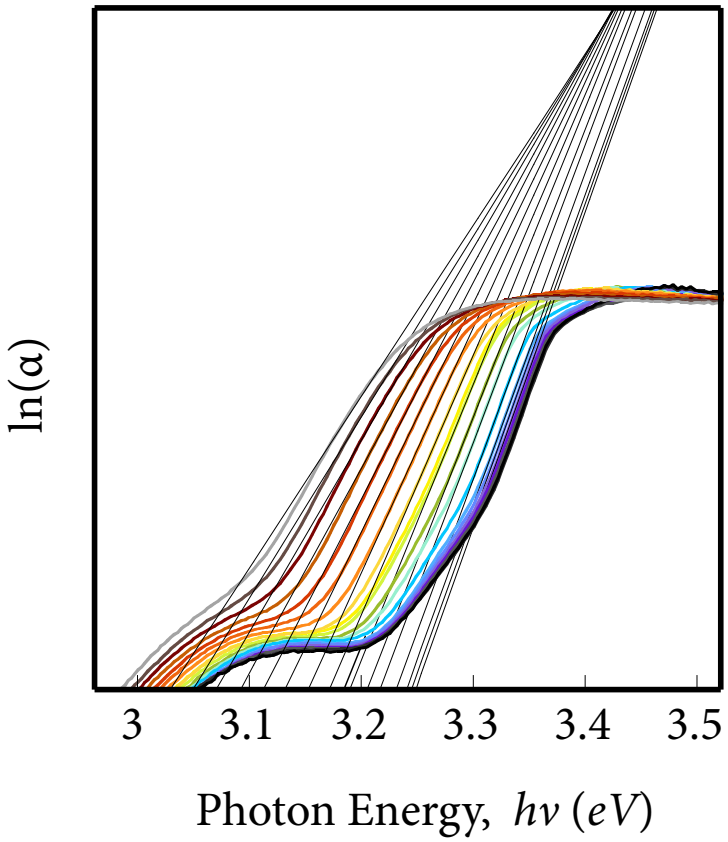

FIGURE 4.15: *Urbach analysis of ZnO as a function of temperature. The Urbach energy parameter is given by the inverse slope at the band edge in a semilogarithmic plot of absorption versus photon energy.*

TABLE 4.2: *Values of the optical gap determined via derivative analysis and values of the Urbach energy parameter, E_u, determined via the "inverse-slope method" as a function of temperature ranging from 77 K–527 K.*

Temp. (K)	$E_g \pm 0.005$ (eV)	$E_u \pm 2$(meV)
77	3.32	29.7
92	3.33	29.4
107	3.33	29.5
122	3.32	29.6
137	3.32	29.5
152	3.32	29.8
167	3.31	30.0
197	3.30	30.5
227	3.30	31.4
257	3.28	32.4
287	3.26	33.7
294	3.26	34.4
317	3.25	35.8
347	3.24	38.0
377	3.23	40.5
407	3.21	42.9
437	3.20	45.6
467	3.18	48.9
497	3.17	51.5
527	3.15	54.4

Conclusion — In this chapter we explored various analytic techniques used to obtain information about the band structure of semiconductor samples through absorption spectra. These techniques give us information about the bandgap of our semiconductors as well as information on the band-edge region. The key parameter of this work is the Urbach energy parameter which allows us to quantify the density of in-gap states for both ZnO and the $Mg_{0.07}Zn_{0.93}O$ alloy.

REFERENCES

[1] J. I. Pankove, *Optical processes in semiconductors* (Prentice-Hall, Englewood Cliffs, NJ, 1971).

[2] L. H. Hall, J. Bardeen, and F. J. Blatt, Physical Review **95**, 559 (1954).

[3] W. Wei, C. Jin, J. Narayan, and R. J. Narayan, Journal of Applied Physics **107** (2010), 10.1063/1.3271415.

[4] B. K. Ridley, *Quantum Processes in Semiconductors* (OUP Oxford, 1999).

[5] H. Che, *Band gaps by design : Tailoring ZnO based semiconductor alloy films*, Ph.D. thesis (2014).

[6] B. Ullrich, C. Zhang, E. F. Schubert, J. E. Cunningham, and K. v. Klitzing, Physical Review B **39**, 3776 (1989).

[7] R. Viswanatha, S. Chakraborty, S. Basu, and D. D. Sarma, The Journal of Physical Chemistry B **110**, 22310 (2006).

[8] M. Wang, E. Kim, S. Kim, J. Chung, I. Yoo, E. Shin, S. Hahn, and C. Park, Thin Solid Films **516**, 1124 (2008).

[9] B. D. Fahlman, *Materials Chemistry* (Springer Science & Business Media, 2007).

[10] M. Willander, O. Nur, J. R. Sadaf, M. I. Qadir, S. Zaman, A. Zainelabdin, N. Bano, and I. Hussain, Materials **3**, 2643 (2010).

[11] F. K. Shan, G. X. Liu, W. J. Lee, and B. C. Shin, Journal of Applied Physics **101**, 053106 (2007).

[12] L. Irimpan, D. Ambika, V. Kumar, V. P. N. Nampoori, and P. Radhakrishnan, Journal of Applied Physics **104**, 033118 (2008).

[13] H. S. Kang, J. S. Kang, J. W. Kim, and S. Y. Lee, Journal of Applied Physics **95**, 1246 (2004).

[14] C. Tsakonas, W. Cranton, F. Li, K. Abusabee, A. Flewitt, Demosthenes Koutsogeorgis, and R. Ranson, Journal of Physics D: Applied Physics **46**, 095305 (2013).

[15] Y. G. Wang, S. P. Lau, X. H. Zhang, H. H. Hng, H. W. Lee, S. F. Yu, and B. K. Tay, Journal of Crystal Growth **259**, 335 (2003).

[16] V. Gupta and A. Mansingh, Journal of Applied Physics **80**, 1063 (1996).

[17] V. Srikant and D. R. Clarke, Journal of Applied Physics **83**, 5447 (1998).

[18] W. S. Shi, O. Agyeman, and C. N. Xu, Journal of Applied Physics **91**, 5640 (2002).

[19] V. V. Khomyak, M. M. Slyotov, I. I. Shtepliuk, G. V. Lashkarev, O. M. Slyotov, P. D. Marianchuk, and V. V. Kosolovskiy, Journal of Physics and Chemistry of Solids **74**, 291 (2013).

[20] S.-Y. Chu, W. Water, and J.-T. Liaw, Journal of the European Ceramic Society **23**, 1593 (2003).

[21] A. K. Viswanath, J. I. Lee, D. Kim, C. R. Lee, and J. Y. Leem, Physical Review B **58**, 16333 (1998).

[22] J. F. Muth, R. M. Kolbas, A. K. Sharma, S. Oktyabrsky, and J. Narayan, Journal of Applied Physics **85**, 7884 (1999).

CHAPTER 5

Analysis of the Temperature Dependent Urbach Energy

Introduction — In this chapter we analyze the band-edge structure as a function of temperature. Various models outlined herein have allowed the quantification of the band-edge using two criteria; firstly, its dependence on defects and secondly, its dependence on thermal fluctuation of the exciton level. It will be shown that the band-edge region of ZnO and $Mg_{0.07}Zn_{0.93}O$ have differing dependence on these two contributions.

5.1 Bose-Einstein oscillator model of electron-phonon interaction

The Bose-Einstein oscillator is used to model the temperature dependence of the optical gap. Since temperature is directly related to the phononic activity in a semiconductor, we begin a derivation of the model with the quantized energy of a phonon of angular frequency ω. Thus, the energy of a vibrational mode is given by:

$$\epsilon = (n + \frac{1}{2})\hbar\omega \tag{5.1}$$

where the mode can be excited to a principal quantum number, n.

The quantity n can be thought of as the number of independent normal phonon modes. The quantity $\frac{1}{2}\hbar\omega$ is the zero-point energy of the mode. It occurs for both phonons and photons as a consequence of their equivalence.

Statistically speaking, a thermally excited environment leads to an increase in the phonon population and causes a wider distribution of absorption events to take place. To model the average distribution of electrons undergoing excitation by n phonon modes we use the partition function, Z, from statistical mechanics. We are required

to normalize the probabilities of thermal excitation as being equal to the sum over all Boltzmann factors.

$$\begin{aligned} Z &= \sum_{n=0}^{\infty} \exp^{-n\hbar\omega/k_B T} = \sum x^n \text{ geometric series for x<1} \\ &= \frac{1}{1 - e^{-\hbar\omega/k_B T}} \end{aligned} \tag{5.2}$$

Thus the probability of occupation is given by the normalized density function:

$$P(n) = \frac{\exp^{-n\hbar\omega/k_B T}}{Z} \tag{5.3}$$

So the average thermal occupancy of $< n >$, or the average distribution of phonon modes of vibration at any given temperature, is:

$$< n >= \sum_{n=0}^{\infty} nP(n) = Z^{-1} \sum n \times \exp^{-n\hbar\omega/k_B T} \tag{5.4}$$

which yields the Bose-Einstein distribution function as follows:

$$< n >= \frac{1}{e^{\hbar\omega/k_B T} - 1} \tag{5.5}$$

The Bose-Einstein model of electron-phonon interaction relates the average distribution of phonon modes to the likelihood of absorption. Thus, the relation is used to model the temperature dependence of the optical gap energy, $E_g(T)$, and is given by the empirical model of the following form:[1,2]

$$E_g(T) = E_o - \frac{2\alpha}{e^{\hbar\omega/k_B T} - 1} \tag{5.6}$$

where E_o is the optical gap energy at o K, α is a coefficient to the Bose-Einstein factor that quantifies the magnitude of electron-phonon coupling and $\Theta_E = \hbar\omega/k_B$

relates the average phonon frequency to the average phonon (Einstein) temperature of the solid.

The increased probability of absorption events at higher temperatures is commonly referred to as "phonon-assisted absorption." Thus, phonon energy contributes directly to red-shifting the optical gap at temperatures above 0 K as shown by experimental data in Figs. 5.1 and 5.2.

Fig. 5.1 and Fig. 5.2 show the experimental data of the temperature dependent optical bandgap and temperature dependent exciton peak of ZnO and $Mg_{0.07}Zn_{0.93}O$. The dotted lines indicates the best fit to the model in Eq. 5.6. Tab. 5.1 shows the parameters obtained by the best fit to the model.

The table shows that the peak energy of excitons at 0 K are higher in energy than that of the optical gap at 0 K, which is reasonable, since the optical gap, especially at absolute zero, is largely due to defect states at lower energies. The electron-phonon coupling, represented by the quantity α, is seen to be less when applied to excitonic resonance than for optical gap transitions. In agreement with this, the average phonon temperature, Θ_E, also decreases for excitonic resonance peaks.

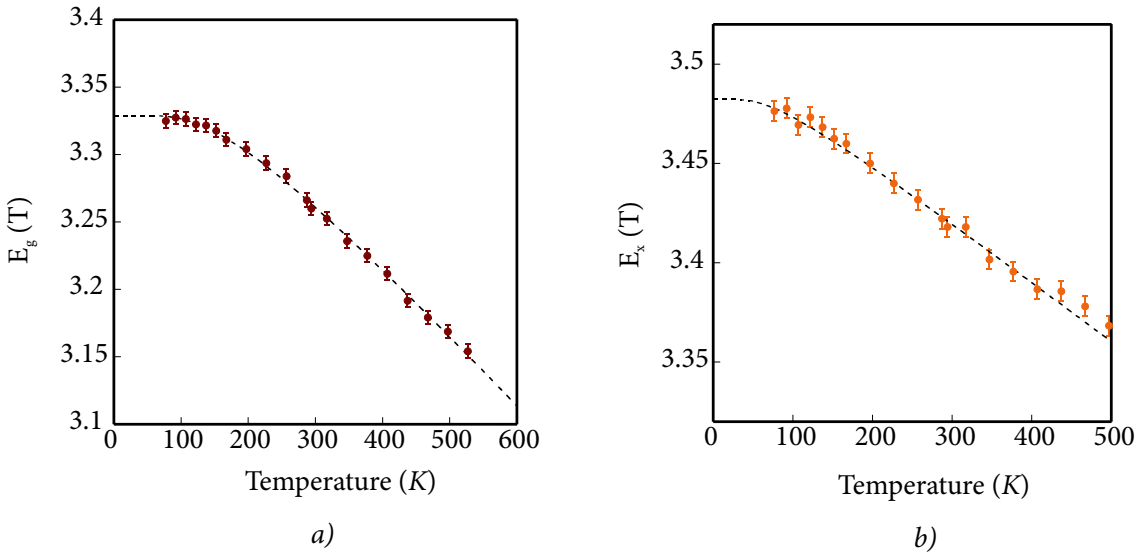

FIGURE 5.1: *The Bose-Einstein Oscillator model of electron-phonon interaction applied to ZnO at (a) the optical gap (b) at the exciton resonance peak.*

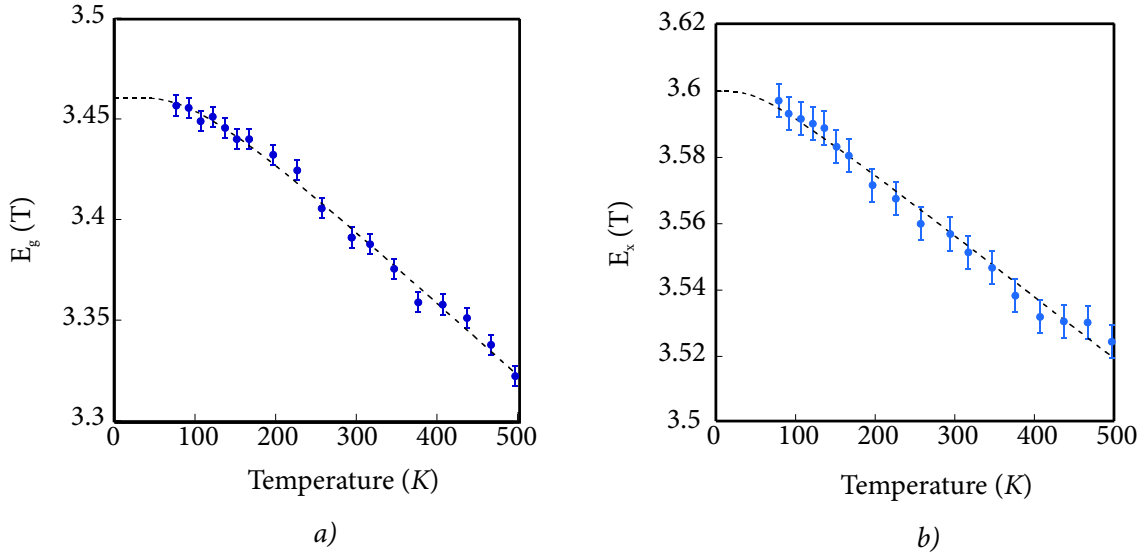

FIGURE 5.2: *The Bose-Einstein Oscillator model of electron-phonon interaction applied to $Mg_{0.07}Zn_{0.93}O$ near (a) the optical gap region and (b) at the exciton resonance peak.*

TABLE 5.1: *The parameters of the best fit to the Bose-Einstein oscillator model of electron-phonon interaction of the data presented in Figures 5.1 & 5.2. The model was applied to both the exciton resonance peak and to the optical gap.*

		E_o (eV)	α (meV)	Θ_E (K)	$\hbar\omega$ (meV)
ZnO	E_x	3.48	30	207	17.8
	E_g	3.33	125	461	39.7
MgZnO	E_x	3.60	14	147	12.6
	E_g	3.46	52	282	24.3

TABLE 5.2: *Values of the adjustable parameters Θ_E, the average phonon temperature, and α, the electron-phonon coupling constant, obtained from a fit of exciton resonance peak energies, E_x, as a function of temperature to the Bose-Einsten model of electron-phonon interaction for ZnO. The tables compares the parameters found in this work to those found in literature.*

Method	Morphology		Model parameters	
			Θ_E (K)	α (meV)
Absorption	Thin Film	Rai[3]	280	24
		This Work	207	30
PL	Bulk	Chen[4]	212	46
		He[5]	264	53
		Boemore[6]	203	50

As shown in Tab. 5.2, the values for the electron-phonon coupling parameter, α, and the average phonon temperature, Θ_E, for ZnO agree well with those found in literature. Values for these parameters agree reasonably well for absorption spectroscopy and photoluminescence spectroscopy as well as for thin film and bulk morphologies. Furthermore, the temperature dependence of E_g more accurately reflects the temperature dependence of the optical gap and will be used in further Urbach analysis of the band-edge.

5.2 TEMPERATURE DEPENDENT URBACH MODELS

Building on the temperature-independent Urbach energy model of band tail transitions given in Eq. 4.13, the temperature dependent Urbach energy model is given by:

$$\alpha(\hbar\omega) = \alpha_o e^{\frac{\sigma(T)(\hbar\omega - E_g)}{k_B T}} \tag{5.7}$$

where

$$E_u(T) = \frac{k_B T}{\sigma(T)} \tag{5.8}$$

where k_B is the Boltzmann factor, T is the temperature and $\sigma(T)$ is the temperature dependent statistical distribution of uniform microfields given by Dow & Redfield.

5.2.1 *Dow & Redfield Model: Exciton-Phonon Interaction*

The phenomenological model by Dow & Redfield of the temperature dependent Urbach energy corresponds theoretically to a thermal average over potential fluctuations of a harmomonic lattice in the dispersionless approximation ($k = 0$) with first-order exciton-phonon interactions and is given by:[7]

$$\sigma(T) = \sigma_o(2k_B T/\hbar\omega) tanh(\hbar\omega/2k_B T) \tag{5.9}$$

where $\hbar\omega$ is suggested to be the energy of phonons involved in broadening the absorption edge and σ_o is a material- dependent parameter that is proportional to slope of the band-edge.

In essence, Dow & Redfield models band-edge broadening as a result of potential fluctuations by an internal Franz-Kieldish effect, concurring with the discussion presented in Sec. 4.7.[8] [4]

[4]The Franz-Keldysh effect is a change in optical absorption by a semiconductor when an electric field is applied.

The model is applied to the data presented in Tab. 4.2 after solving for $\sigma(T)$ from Eq. 5.8.

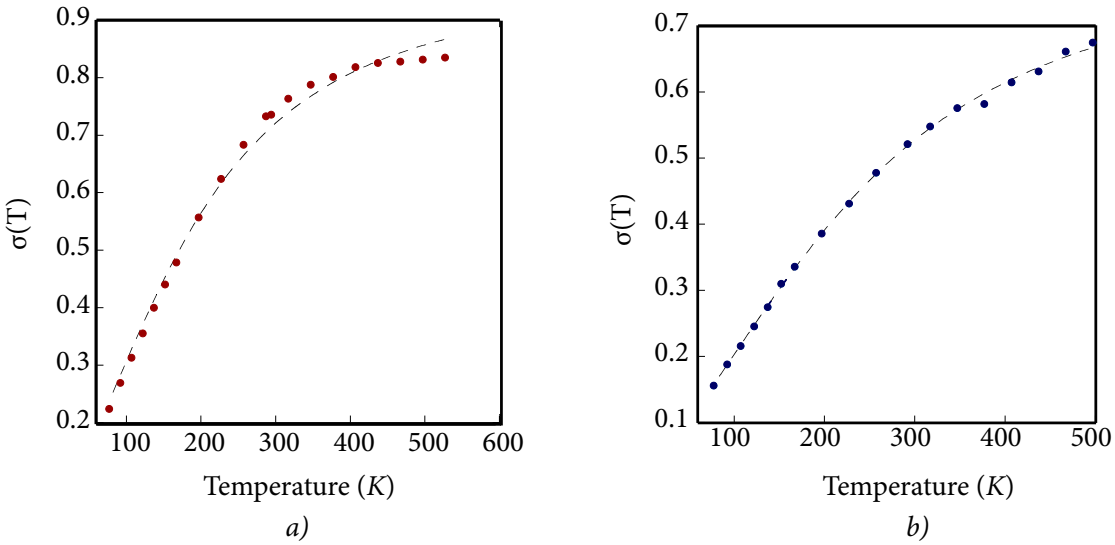

FIGURE 5.3: *The Dow & Redfield model of $\sigma(T)$ (Eq. 5.9) applied to (a) ZnO & (b) $Mg_{0.07}Zn_{0.93}O$. The best fit yields the steepness parameter σ_o and the average phonon frequency of the material, $\hbar\omega$.*

Fig. 5.3 shows the result of the Dow & Redfield analysis of the temperature dependent sigma parameter in ZnO and $Mg_{0.07}Zn_{0.93}O$ and the results of the best fit to the model are shown in Tab. 5.3.

TABLE 5.3: *The best fit to the Dow & Redfield model of the data presented in Figure 5.3. The model was applied to ZnO & $Mg_{0.07}Zn_{0.93}O$ and yields the steepness parameter σ_o and the average phonon frequency of the material, $\hbar\omega$. The right-most column represents the average phonon frequency as temperature.*

	σ_o	$\hbar\omega$ (meV)	Θ (K)
ZnO	0.97	54	626
MgZnO	0.80	68	789

The model fits the data well, however, literature shows that the value of Θ given by the Dow & Redfield model may be over-reported. In some extreme cases, the average phonon frequency has been observed to be significantly greater than the

highest available phonon frequency given by phonon dispersion plots. This has been purported by Wasim et al and others to be due to the presence of defects.[9,10]

Further analysis of the temperature dependent Urbach energy parameter supports this assertion, as will be shown presently.

5.2.2 *Wasim Model*

Wasim proposes that the over-reported values of Θ in the Dow & Redfield model are due to the presence of defects, which the model does not distinguish from strictly phononic contributions to the band edge. In essence, the model treats all potential fluctuations—both static and dynamic—equally.[9,11]

Wasim proposes a new model of the temperature dependent Urbach energy that accounts for phonon interactions as well as defects and is given by:

$$E_u(T,P,N) = \left(\frac{k_B\Theta}{\sigma_o}\right)\left[\frac{1+P}{2} + \frac{N}{e^{\Theta/T}-1}\right] \tag{5.10}$$

where k_B is the Boltzmann constant, Θ is the average phonon temperature, σ_o is the steepness parameter described previously, P is a parameter proportional to the concentration of defect states, and the numerator in the Bose-Einstein-type factor, N, is proportional to the occupancy of available phonon modes.

P lies between zero and one, and $P = 0$ indicates perfect crystal structure. The numerator in the Bose-Einstein factor, N, lies between zero and one—"1" indicating occupancy of all available phonon modes.[3]

As a quick check that defects contribute to the over-reported value of Θ, we can specify σ_o, obtained from the Dow & Redfield model, and set $P = 0$ (assuming perfect crystallinity) in the Wasim model. This configuration yields $N \approx 1$ as shown in Tab. 5.4 by values corresponding to the "Wasim ('mod'ified.)" model. Furthermore,

following this criteria, the average phonon temperature of the Wasim model yields approximately that given by the Dow & Redfield model.

Similarity of the average phonon temperature, Θ, between these models implies that it is very likely the Dow & Redfield model assumes perfect crystallinity and occupancy of all available phonon modes leading to the over-reported value of Θ.

Continuing with further Urbach Analysis to separate the contribution of defects and phonon broadening to the band-edge, requires the use of a reasonable value of Θ, which is given in Tab. 5.1. This value of Θ pertains to E_g, the optical gap.[1,12,13]

As will be shown presently, this Θ gives reasonable values for P and N—values that do not indicate perfect crystallinty ($P \neq 0$) and less than one-hundred percent occcupancy of phonon modes ($N \neq 1$), in either ZnO or $Mg_{0.07}Zn_{0.93}O$, as can be expected. Fitting the temperature-dependent Urbach energy under these conditions, we obtain reasonable values for P and N as shown in Tab. 4.2. The fit is indicated by the solid line in Fig. 5.2

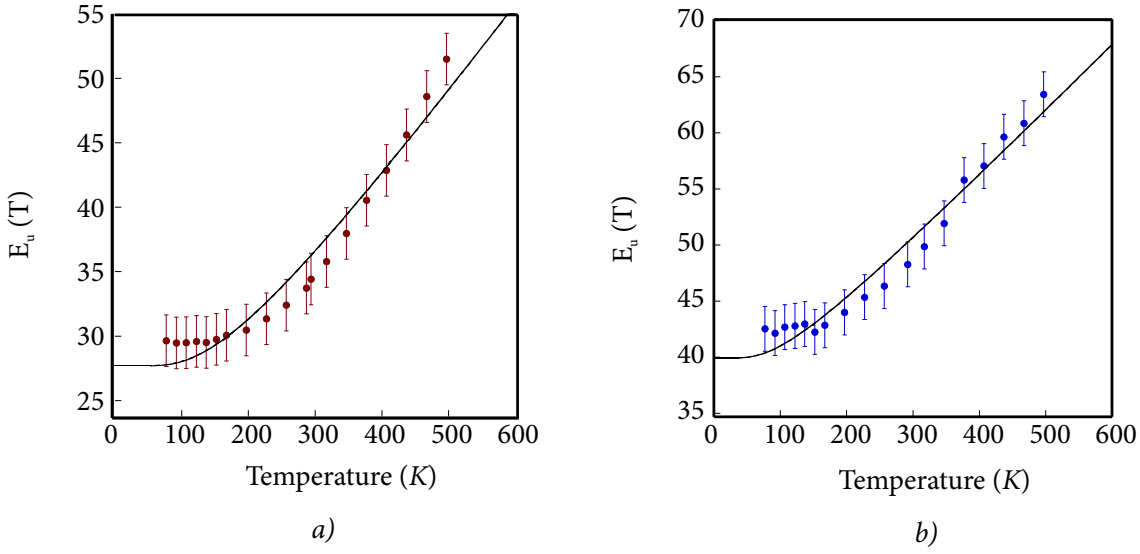

FIGURE 5.4: *The Urbach energy parameter as a function of temperature in ZnO & MgZnO. The solid line shows a fit to the Wasim model, where P & N are variables.*

Describing the band-edge of ternary semiconductors with a larger concentration of structural defects is a more formidable problem than describing the band-edge of

TABLE 5.4: *Parameters obtained by fitting the temperature dependent Urbach Energy to the modified (mod.) Wasim, Wasim & Dow & Redfield model of the temperature-dependent exponential absorption tail. The parameters denoted by "†" were specified for the fit. Θ is the average phonon temperature, σ_o is the steepness parameter, P is a parameter proportional to the concentration of defect states, and N, is proportional to the occupancy of available phonon modes.*

		$\sigma_o{}^{\dagger}$	Θ (K)	$\hbar\omega$ (meV)	P	N
ZnO	Wasim (mod.)	0.97	642	55	$0^{\dagger}$	0.98
	Wasim	0.97	$461^{\dagger}$	40	0.34	0.79
	Dow & Redfield	0.97	626	54	–	–
MgZnO	Wasim (mod.)	0.80	787	68	$0^{\dagger}$	0.99
	Wasim	0.80	$282^{\dagger}$	24	1.62	0.55
	Dow & Redfield	0.80	789	68	–	–

single-element or binary semiconductors and more robust models than that given by Dow & Redfield are required.[9,11] As a final verification that assuming $P = 0$ will reflect on $\hbar\omega$ as an increase in the phonon temperature observed, the $Mg_{0.07}Zn_{0.93}O$ alloy shows an average phonon frequency that is over-reported by approximately 44 *meV*, whereas ZnO only displays an average phonon frequency that is over-reported by approximately 15 *meV*, shown in Fig. 5.4. This is reasonable since we expect to see a higher defect presence in $Mg_{0.07}Zn_{0.93}O$ than in ZnO.

To bring the discussion of details of the models to a close, the steepness parameter, σ_o can be specified in the Wasim model of the temperature-dependent Urbach energy using the Dow & Redfield model, while the value of Θ is specified by the electron-phonon model of the optical gap. This yields reasonable values for P and N.

The physical interpretation of the results of fitting the Wasim model to the temperature-dependent Urbach energy can be summarized as follows. At 77 *K*, in the absence of phonon broadening, we obtain a baseline for structural defect concentration indicated by the parameter P. P for ZnO was found to be 0.34 while P for $Mg_{0.07}Zn_{0.93}O$ was found to be 1.62. Absorption events below the fundamental gap in this temperature regime can be mostly attributed to defects. Any further absorption which occurs from

increasing temperature thereafter can be attributed to phonon broadening. The *degree* to which absorption increases from the defect baseline as temperature is increased, gives the parameter N, which is related to the exciton-phonon coupling. N for the $Mg_{0.07}Zn_{0.93}O$ alloy is less than that for ZnO, 0.55 as compared to 0.79, shown in Tab. 5.4. Comparing respective values of α, the exciton-phonon coupling, given in Tab. 5.1 corroborate this relationship nicely—that is, 30 *meV* in ZnO in comparison to 14 *meV* for $Mg_{0.07}Zn_{0.93}O$.

Conclusion — In this chapter we have seen that both the defect-dependence and temperature-dependence of the band-edge region were altered in ZnO by alloying to obtain $Mg_{0.07}Zn_{0.93}O$. By using models found throughout literature—the Dow & Redfield and Wasim models—we have a relative measure of the contribution of phonon broadening and defects to intrinsic ZnO and the $Mg_{0.07}Zn_{0.93}O$ alloy. The results indicate that the $Mg_{0.07}Zn_{0.93}O$ alloy has a higher defect contribution to the band-edge than ZnO—1.62 versus 0.34, respectively. Furthermore, the $Mg_{0.07}Zn_{0.93}O$ alloy is shown to have a lower phonon interaction near the band-edge region as compared to ZnO—0.55 versus 0.79. These results will be further discussed in the following chapter.

REFERENCES

[1] L. Malikova, W. Krystek, F. H. Pollak, N. Dai, A. Cavus, and M. C. Tamargo, Physical Review B **54**, 1819 (1996).

[2] P. Lautenschlager, M. Garriga, L. Vina, and M. Cardona, Physical Review B **36**, 4821 (1987).

[3] R. C. Rai, Journal of Applied Physics **113**, 153508 (2013).

[4] X.-B. Chen, J. Huso, J. L. Morrison, and L. Bergman, Journal of Applied Physics **102**, 116105 (2007).

[5] H. P. He, Z. Z. Ye, S. S. Lin, H. P. Tang, Y. Z. Zhang, L. P. Zhu, J. Y. Huang, and B. H. Zhao, Journal of Applied Physics **102**, 013511 (2007).

[6] C. Boemare, T. Monteiro, M. J. Soares, J. G. Guilherme, and E. Alves, Physica B: Condensed Matter International Conference on Defects in Semiconductors, **308—310**, 985 (2001).

[7] J. D. Dow and D. Redfield, Physical Review B **5**, 594 (1972).

[8] A. Iribarren, R. Castro-Rodríguez, V. Sosa, and J. L. Peña, Physical Review B **60**, 4758 (1999).

[9] S. M. Wasim, C. Rincón, G. Marín, P. Bocaranda, E. Hernández, I. Bonalde, and E. Medina, Physical Review B **64**, 195101 (2001).

[10] E. M. Ismardo Bonalde, Phys. Rev. B **69** (2004), 10.1103/PhysRevB.69.195201.

[11] C. Rincón, S. M. Wasim, G. Marín, R. Márquez, L. Nieves, G. S. Pérez, and E. Medina, Journal of Applied Physics **90**, 4423 (2001).

[12] R. Pä ssler, E. Griebl, H. Riepl, G. Lautner, S. Bauer, H. Preis, W. Gebhardt, B. Buda, D. J. As, D. Schikora, K. Lischka, K. Papagelis, and S. Ves, Journal of Applied Physics **86**, 4403 (1999).

[13] S. R. Johnson and T. Tiedje, Journal of Applied Physics **78**, 5609 (1995).

CHAPTER 6

Discussion & Conclusion

6.1 discussion of experimental analysis

Several changes have been observed following the introduction of Mg as a substitutional impurity to ZnO. Broadly speaking, these changes can be categorized as defect-related and exciton-broadening related. These categories will be addressed separately followed by a brief discussion of possible relationships between the two.

To summarize results from experimental analysis, we observe reduced phonon broadening of the exciton peak in MgZnO relative to that of ZnO. This is reflected in the parameter N in Tab. 5.4. In parallel, parameter α given in Tab. 5.1, indicates reduced exciton-phonon coupling in the alloy. Furthermore, the average phonon temperature of the alloy, given by Θ, indicates a lower over-all phonon population within the sample.

To understand the source of the decrease in phonon broadening we first consider the excitonic changes incurred by alloying. The binding energies of excitons in MgO and ZnO are approximately 100 meV and 60 meV, respectively. In the ternary compound MgZnO we may expect the excitonic binding energy to increase from 60 meV and lie somewhere between that of both end-members.[1,2]

Experiments by Sun et al. showed a significant increase in excitonic binding energy by decreasing well-width in ZnO/MgZnO multiquantum wells.[3] Furthermore, this enhancement of excitonic binding energy increased in proportion to Mg concentration. Consequently, Sun et al. observed an inverse relationship between excitonic binding energy and exciton-phonon coupling and concluded that the decreased coupling be attributed to the enhanced excitonic binding energy. It has been suggested that optical phonons give rise to dynamical screening of the electron-hole Coulomb interaction.

So, it stands to reason, that a higher exciton binding energy ultimately resists interaction with phonons more strongly.[4,5]

However, in thin films, numerous reports have shown exciton binding energies of MgZnO alloys to be roughly the same if not slightly less than that of ZnO.[6–10]Thus, while an increase in excitonic binding energy in multiquantum wells contributes to decreased phonon broadening, in the thin film studied in this work, the decrease in broadening would not be attributed to an increase in excitonic binding energy.

Next we consider the effect of exciton localization. Due to the inherent nature of alloying, substitutional atoms could possibly not be homogeneously distributed throughout the MgZnO alloy leading to Zn-rich or Mg-rich domains.[1] This is known as compositional fluctuation. This alloy-induced disorder has been reported to be the main mechanism for exciton localization in MgZnO alloys.[11,12]

It is reasonable then that exciton localization be strongly considered as playing a significant role in decreasing the effects of phonon broadening.

In regard to structural changes incurred in our alloy, we must first rule out the possibility of a change in crystal symmetry. Well below the phase segregation region, Mg does not alter the overall crystal symmetry of the sample and the wurtzite structure remains in equilibrium. Perhaps the most significant structural change between ZnO and the MgZnO alloy is the introduction of structural defects. According to parameters given by the Wasim model, we observe an 80-percent increase in structural defect concentration from ZnO to MgZnO. It is well known that alloying may also lead to an increased presence of structural defects within the crystal,[13] which may include dislocations and grain boundaries. In this discussion we focus on grain boundaries, which have been shown to affect the electronic properties of semiconductors. Studies of grain boundaries via quantum mechanical calculations by McKenna et al. have shown that grain boundaries may trap electrons and holes, owing to both their intrinsic electronic structure, i.e. strong local potentials, and because there are

often enhanced concentrations of electronically active defects segregated there.[14] The study modeled electron/hole trapping in MgO and showed that trapped electrons are confined inside the open channels at the grain boundary. Given the possible increase in grain boundaries in MgZnO, indicated in the models, similar mechanisms may be in place. It is reasonable to suppose that excitons are trapped in much the same way in MgZnO grain boundaries as in the case of alloy-induced disorder; that is, by the strong perturbation in localized fields there.

The presence of trapped excitons may not themselves directly contribute to the reduced phonon broadening in the MgZnO alloy, but perhaps offer an indication of the mechanism at play. It is well accepted that intrinsic lattice disorder leads to a decrease in phonon lifetime. In essence, phononic propagation may be interrupted by the decrease in long range periodicity within the alloy. Consequently, one observable effect of this phenomenon may lie in the reduced exciton-phonon interaction in trapped excitons at grain boundaries. This is likely due the statistically negligible eventuality of encountering the influence of phonons there.

The hypothesis formed via investigation of the MgZnO alloy can be applied in-turn to the intrinsic ZnO studied here. The P-value of ZnO was found to be 0.34, less than that of MgZnO at 1.62. Consequently, we expect to see, in light of our assertions, an increased efficiency in thermal broadening due to improvement in crystal quality. Thus, the value of N in ZnO is increased relative to that of MgZnO—increasing to 0.79 from 0.55, respectively.

Conclusion — We can conclude that the decrease in exciton-phonon interactions observed in MgZnO relative to ZnO is very likely attributable to structural defects which may in turn cause formation of localized excitons. Furthermore, these localized excitons are proposed to encounter phonons with correspondingly decreased likelihood due to the diminished phonon lifetime in a disordered lattice.

6.2 FUTURE WORK

Future work should investigate the nature of defects in the MgZnO alloy, accomplished through complementary spectroscopy such as photoluminescence. The MgZnO alloy likely possesses Mg-related defects that are largely unknown.

REFERENCES

[1] T. A. Wassner, B. Laumer, S. Maier, A. Laufer, B. K. Meyer, M. Stutzmann, and M. Eickhoff, Journal of Applied Physics **105**, 023505 (2009).

[2] J. F. Kong, W. Z. Shen, Y. W. Zhang, C. Yang, and X. M. Li, Applied Physics Letters **92**, 191910 (2008).

[3] H. D. Sun, T. Makino, Y. Segawa, M. Kawasaki, A. Ohtomo, K. Tamura, and H. Koinuma, Journal of Applied Physics **91**, 1993 (2002).

[4] A. K. Viswanath, J. I. Lee, D. Kim, C. R. Lee, and J. Y. Leem, Physical Review B **58**, 16333 (1998).

[5] P. D. M. Ueta, P. D. H. Kanzaki, P. D. K. Kobayashi, P. D. Y. Toyozawa, and P. D. E. Hanamura, in *Excitonic Processes in Solids*, Springer Series in Solid-State Sciences No. 60 (Springer Berlin Heidelberg, 1986) pp. 203–284.

[6] J. S. Hong, S. W. Ryu, W. P. Hong, J.-J. Kim, H.-M. Kim, and S.-H. Park, in *Nanotechnology Materials and Devices Conference, 2006. NMDC 2006. IEEE*, Vol. 1 (IEEE, 2006) pp. 324–325.

[7] C. W. Teng, J. F. Muth, U. Ozgur, M. J. Bergmann, H. O. Everitt, A. K. Sharma, C. Jin, and J. Narayan, Appl. Phys. Lett **76**, 979 (2000).

[8] M. D. Neumann, C. Cobet, N. Esser, B. Laumer, T. A. Wassner, M. Eickhoff, M. Feneberg, and R. Goldhahn, Journal of Applied Physics **110**, 013520 (2011).

[9] A. MÃijller, G. Benndorf, S. Heitsch, C. Sturm, and M. Grundmann, Solid State Communications **148**, 570 (2008).

[10] R. Schmidt, B. RheinlÃd'nder, M. Schubert, D. Spemann, T. Butz, J. Lenzner, E. M. Kaidashev, M. Lorenz, A. Rahm, H. C. Semmelhack, and M. Grundmann, Applied Physics Letters **82**, 2260 (2003).

[11] M. Karaliunas, E. Kuokstis, S.-Y. Ting, J.-J. Huang, and C. C. Yang, Journal of Applied Physics **116**, 123501 (2014).

[12] J. D. Ye, K. W. Teoh, X. W. Sun, G. Q. Lo, D. L. Kwong, H. Zhao, S. L. Gu, R. Zhang, Y. D. Zheng, S. A. Oh, X. H. Zhang, and S. Tripathy, Applied Physics Letters **91**, 091901 (2007).

[13] D. Thapa, J. Huso, H. Che, M. Huso, J. L. Morrison, D. Gutierrez, M. Grant Norton, and L. Bergman, Applied Physics Letters **102**, 191902 (2013).

[14] K. P. McKenna and A. L. Shluger, Proceedings of the Royal Society of London A: Mathematical, Physical and Engineering Sciences **467**, 2043 (2011).